JGR Solid Earth

RESEARCH ARTICLE
10.1029/2019JB017530

Gravitational Changes of the Earth's Free Oscillation From Earthquakes: Theory and Feasibility Study Using GRACE Inter-satellite Tracking

Khosro Ghobadi-Far[1], Shin-Chan Han[1], Jeanne Sauber[2], Frank Lemoine[2], Saniya Behzadpour[3], Torsten Mayer-Gürr[3], Nico Sneeuw[4], and Emile Okal[5]

[1]School of Engineering, University of Newcastle, Callaghan, New South Wales, Australia, [2]Geodesy and Geophysics Lab, NASA Goddard Space Flight Center, Greenbelt, MD, USA, [3]Institute of Geodesy, Graz University of Technology, Graz, Austria, [4]Institute of Geodesy, University of Stuttgart, Stuttgart, Germany, [5]Department of Earth and Planetary Sciences, Northwestern University, Evanston, IL, USA

Key Points:
- Earth's free oscillations excited by great earthquakes cause transient global gravity changes that perturb the GRACE orbital trajectory
- We develop an analytic model of inter-satellite range perturbation caused by the Earth's free oscillations
- Wavelet analysis of GRACE data reveals a candidate for *football* mode excited by 2004 Sumatra earthquake but obscured by accelerometer error

Supporting Information:
- Supporting Information S1

Correspondence to:
K. Ghobadi-Far,
khosro.ghobadifar@uon.edu.au

Citation:
Ghobadi-Far, K., Han, S.-C., Sauber, J., Lemoine, F., Behzadpour, S., Mayer-Gürr, T., et al. (2019). Gravitational changes of the Earth's free oscillation from earthquakes: Theory and feasibility study using GRACE inter-satellite tracking. *Journal of Geophysical Research: Solid Earth*, *124*, 7483–7503. https://doi.org/10.1029/2019JB017530

Received 14 FEB 2019
Accepted 19 MAY 2019
Accepted article online 28 MAY 2019
Published online 30 JUL 2019

Abstract GRACE satellites have detected regional-scale preseismic, coseismic, and postseismic gravity changes associated with great earthquakes during the GRACE era (2002-2017). Earthquakes also excite global-scale transient gravity changes associated with free oscillations that may be discerned for a few days. In this study, we examine such global gravity changes due to Earth's free oscillations and quantify how they affect GRACE measurements. We employ the normal mode formalism to synthesize the global gravity changes after the 2004 Sumatra earthquake and simulate the (gravitational) free oscillation signals manifested in the GRACE K-band ranging (KBR) measurements. Using the Kaula orbit perturbation theory, we show how GRACE inter-satellite distances are perturbed through a complex coupling of eigenfrequencies of the normal modes with the Earth's rotation rate and the GRACE satellites' orbital frequency. It is found that a few gravest normal modes can generate range-rate perturbations as large as 0.2 μm/s, which are comparable to actual errors of GRACE KBR ranging and accelerometer instruments. Wavelet time-frequency analysis of the GRACE KBR residual data in December 2004 reveals the existence of a significant transient signal after the 2004 Sumatra earthquake. This transient signal is characterized by a frequency of ~0.022 mHz that could be potentially associated with the largest excitation due to the "football" mode of the Earth's free oscillation. However, the results are also affected by low-frequency noise of the GRACE accelerometers. Improved space-borne gravitational instrumentation may open new opportunities to study the Earth's interior and earthquakes independently from global seismological analysis.

1. Introduction

The Gravity Recovery and Climate Experiment (GRACE) mission measured the time-variable gravity field of the Earth with unprecedented spatial and temporal resolutions for more than 15 years from April 2002 to October 2017 (Tapley et al., 2004). By measuring temporal variations of the gravity field, GRACE tracked how terrestrial water, ocean, atmosphere, ice sheets/glaciers, and solid Earth masses are redistributed in the Earth system (e.g., Cazenave & Chen, 2010). The GRACE Follow-On (GRACE-FO) mission, launched on 22 May 2018, is carrying on the legacy of its predecessor with enhanced instrumentation (Webb, 2018).

Earthquakes cause gravity changes by deforming the Earth and changing ambient densities of the crust and mantle. GRACE detected regional-scale coseismic and postseismic gravity changes after recent great (M_w>8.0) earthquakes such as the 2004 Sumatra (Indonesia) earthquake (e.g., De Linage et al., 2009; Han et al., 2006) and the 2010 Maule (Chile) earthquake (e.g., Han et al., 2010; Heki & Matsuo, 2010), as well as strike-slip faulting events such as the 2012 Indian Ocean earthquake (e.g., Han et al., 2015). Furthermore, GRACE detected a migration pattern of gravity changes due to deep and crustal processes a few months prior to the 2011 Tohoku (Japan) earthquake (Panet et al., 2018). Studies of preseismic, coseismic, and postseismic gravity changes from GRACE are based primarily on the analysis of Level-2 (L2) monthly mean solutions of the Earth's gravity field represented in terms of spherical harmonic (SH) coefficients of the geopotential field.

At shorter time scales, earthquakes also yield transient global-scale gravity changes by exciting free oscillations of the Earth. Earth's free oscillations are standing waves that only exist at discrete

frequencies and they are classified into spheroidal and toroidal modes (Woodhouse & Deuss, 2007). Toroidal modes do not yield change in volume (or density) nor radial deformation, and thus, they do not change the Earth's gravitational field. Ground gravimeters were first used to detect the Earth's free oscillations during the 1960 Chilean earthquake (Ness et al., 1961), and more recently, for example, following the 2004 Sumatra earthquake by Rosat et al. (2005). Earth's free oscillations provide a viable source for understanding the internal density structure of the Earth and source mechanism of earthquakes (e.g., Gilbert & Dziewonski, 1975; Masters et al., 1982; Park et al., 2005; Ritzwoller & Lavely, 1995; Stein & Okal, 2005).

Global gravity changes such as from the Earth's free oscillations perturb the orbital trajectory of satellites. The primary aim of this paper is to put forward the principles for modeling and observing such transient gravitational perturbations from GRACE satellites orbiting at ~500 km above the Earth's surface. Our secondary aim is to carry out a thorough feasibility study, using both synthetic and actual data analysis, to see if GRACE could detect the transient perturbations after the great 2004 Sumatra earthquake. Since the Earth's free oscillations are predicted to be detected only for a few days after earthquakes, GRACE L2 monthly mean solutions are not appropriate for studying this problem. Instead, we examine transient gravity changes due to free oscillations manifested in the instantaneous Level-1B (L1B) K-band ranging (KBR) data of the GRACE mission. GRACE KBR data comprise relative orbit perturbations in the form of inter-satellite range, range-rate or range-acceleration between two satellites separated over a distance of ~220 km. We also note that transient gravitational free oscillation signals could contaminate the GRACE gravity and mass redistribution products through aliasing of the high-frequency signals into the monthly mean solutions (e.g., Han et al., 2004).

We use the normal mode summation scheme to model and analyze the gravitational change caused by the Earth's free oscillations (Gilbert, 1970). This scheme has been employed to synthesize the transient seismic waves (e.g., Gilbert & Dziewonski, 1975; Kanamori & Cipar, 1974) and the permanent coseismic deformation (Pollitz, 1996). Similarly, permanent coseismic gravity changes can also be represented by the normal mode summation of gravitational potential (Chao & Gross, 1987; De Linage et al., 2009; Gross & Chao, 2006; Han et al., 2013). In this study, we employ the Earth's normal mode formalism, as introduced for the first time by Chao and Gross (1987), to synthesize the transient gravity signals associated with the free oscillations excited by the great Sumatra earthquake of 26 December 2004, which is the largest earthquake recorded over the GRACE era (2002-2017).

As the principal ingredient of our procedure for studying free oscillations using GRACE satellites, we show how periodic variations in the Earth's gravity field corresponding to normal modes are mapped into the L1B KBR measurements. In other words, we describe how GRACE satellites sample the Earth's free oscillations. To that end, we use the Kaula representation of along-track functionals in terms of orbital coordinates (Kaula, 1966). Our analytic results of the gravitational excitation, as measured by GRACE satellites, are validated by independent numerical orbit integration simulating the along-track perturbations in the GRACE orbital trajectory. Finally, we analyze the actual GRACE KBR data for detecting possible *transient* gravitational changes by the 2004 Sumatra earthquake.

The paper is organized as follows. In section 2, we review the normal mode summation scheme for global gravitational potential changes induced by earthquakes. In section 3, we quantify surface gravity changes in terms of geoid undulation and gravity disturbance. The analytic model of gravitational excitation in the along-track range and range-rate due to free oscillations is derived in section 4. This section also deals with the quantification of along-track perturbations due to the gravest normal modes and their comparison with the GRACE measurement error. Section 6 presents results of analyzing actual GRACE KBR data for possible detection of the low-frequency free oscillation excited by the 2004 Sumatra earthquake. Conclusions are drawn and ongoing, and future gravimetric observations with satellite capabilities are discussed in section 6.

2. Normal Mode Synthesis of Gravitational Potential Change

We describe the excitation of spheroidal modes of the Earth's gravitational potential by an earthquake point source model. As stated earlier, toroidal modes do not excite the gravity field of the Earth. Furthermore, GRACE measurements are not sensitive to gravitational changes of SH degree 0, as

excited by, for example, the "breathing" mode ${}_0S_0$ (e.g., Park et al., 2005), and SH degree 1, as excited by, for example, the Slichter mode ${}_1S_1$ (e.g., Ding & Chao, 2015). Therefore, these modes are not considered in this paper. Han et al. (2013) used the formalism of the Earth's normal modes to study permanent coseismic changes of the gravitational potential after earthquakes. In this paper, we exploit the same formalism to study *transient* gravitational potential changes at seismic frequencies. We start by considering a coordinate frame in which the point source (at radius r_s) is placed at the polar axis and the prime meridian is oriented along the local south. In such a frame, gravitational potential change δV at radius r ($r \geq a$), co-latitude θ, and longitude λ, and at time t after the earthquake is formulated as (Han et al., 2013):

$$\delta V(r,\theta,\lambda,t) = \frac{GM}{a}\sum_{l=0}^{\infty}\left(\frac{a}{r}\right)^{l+1}\sum_{m=0}^{2}P_{lm}(\cos\theta)\{\delta C_{lm}(t)\cos m\lambda + \delta S_{lm}(t)\sin m\lambda\} \tag{1}$$

where SH order m is limited to 0, 1, and 2 for a point source double-couple. In equation (1), a is the radius of the spherical Earth, GM is the product of gravitational constant and the Earth's mass, and P_{lm} is the associated Legendre function of SH degree l and order m.

The time-dependent and dimensionless coefficients $\delta C_{lm}(t)$ and $\delta S_{lm}(t)$ (for $m = 0$, 1 and 2) are obtained by summation of spheroidal modes (eigenfunctions) of all possible overtones n as follows:

$$\delta C_{l0}(t) = \sum_n \delta C_{l0_n} f_l(t) \tag{2a}$$

$$\delta C_{l1}(t) = \sum_n \delta C_{l1_n} f_l(t) \tag{2b}$$

$$\delta S_{l1}(t) = \sum_n \delta S_{l1_n} f_l(t) \tag{2c}$$

$$\delta C_{l2}(t) = \sum_n \delta C_{l2_n} f_l(t) \tag{2d}$$

$$\delta S_{l2}(t) = \sum_n \delta S_{l2_n} f_l(t) \tag{2e}$$

where the time-history function ${}_nf_l(t)$ of each spheroidal mode is defined by

$${}_nf_l(t) = 1 - \cos({}_n\omega_l t)\exp\left(\frac{-{}_n\omega_l t}{2{}_nQ_l}\right) \tag{3}$$

The first term in equation (3; expressed as "1") represents the permanent (gravity) change, while the second term describes the transient oscillation with the eigenfrequency ${}_n\omega_l$ ($=2\pi/{}_nT_l$, where ${}_nT_l$ is the period) and the attenuation factor ${}_nQ_l$ (Aki & Richards, 2002).

Describing the earthquake point source by a deviatoric moment tensor with components (M_{rr}, $M_{r\theta}$, $M_{r\lambda}$, $M_{\theta\theta} - M_{\lambda\lambda}$, and $M_{\theta\lambda}$), the gravitational potential coefficients of each spheroidal mode are obtained as

$${}_n\delta C_{l0} = \frac{a}{GM}\left(\frac{-M_{rr}}{2}\right){}_nP_l(a){}_nK_l^0(r_s) \tag{4a}$$

$${}_n\delta \mathrm{C}_{l1} = \frac{a}{\mathrm{GM}}(\mathrm{M}_{r\theta}){}_nP_l(a)_n K_l^1(r_s) \tag{4b}$$

$${}_n\delta \mathrm{S}_{l1} = \frac{a}{\mathrm{GM}}(M_{r\lambda}){}_nP_l(a)_n K_l^1(r_s) \tag{4c}$$

$${}_n\delta \mathrm{C}_{l2} = \frac{a}{\mathrm{GM}}\left(\frac{M_{\theta\theta}-M_{\lambda\lambda}}{2}\right){}_nP_l(a)_n K_l^2(r_s) \tag{4d}$$

$$ {}_n\delta S_{l2} = \frac{a}{\mathrm{GM}}(M_{\theta\lambda})\,{}_nP_l(a)\,{}_nK_l^2(r_s) \tag{4e} $$

where ${}_nP_l$ is the gravitational potential component of the eigenfunctions, introduced by Alterman et al. (1959) and often given as y_5 in other seismology contributions (e.g., Saito, 1967). In equation (4), we evaluate ${}_nP_l$ at the Earth's surface ($r = a$) so that the set of the SH coefficients represents the geopotential field at $r = a$.

Equation (4) makes use of the excitation functions ${}_nK_l^0$, ${}_nK_l^1$, and ${}_nK_l^2$, respectively, for the source with SH order $m = 0$, $m = 1$, and $m = 2$ (Dahlen, 1980; Nissen-Meyer et al., 2007). They are equivalent to K_0, K_1, and K_2 of Kanamori and Cipar (1974), used to express the vertical displacements of the spheroidal modes. By rewriting the excitation functions in terms of eigenfunctions of vertical and horizontal deformation (${}_nU_l$ and ${}_nV_l$, respectively) and their radial derivatives ($\frac{d_nU_l}{dr}$ and $\frac{d_nV_l}{dr}$) evaluated at the source radius ($r = r_s$), we obtain

$$ {}_nK_l^0(r_s) = \frac{2l+1}{4\pi_nE_l}\left(\frac{2_nU_l(r_s)}{r_s} - \frac{2d_nU_l(r_s)}{dr} - \frac{l(l+1)_nV_l(r_s)}{r_s}\right) \tag{5a} $$

$$ {}_nK_l^1(r_s) = \frac{2l+1}{4\pi_nE_l}\left(\frac{{}_nU_l(r_s)}{r_s} - \frac{{}_nV_l(r_s)}{r_s} + \frac{d_nV_l(r_s)}{dr}\right) \tag{5b} $$

$$ {}_nK_l^2(r_s) = \frac{2l+1}{4\pi_nE_l}\left(\frac{{}_nV_l(r_s)}{r_s}\right) \tag{5c} $$

where the energy integral of each mode is computed in its kinetic form through ${}_nE_l = {}_n\omega_l^2\int_0^a\rho(r)\left\{{}_nU_l^2(r) + l(l+1)_nV_l^2(r)\right\}r^2dr$ with $\rho(r)$ being the radially variable density.

Equations (1) through (5) are exactly identical to the vertical displacement component of spheroidal oscillations U_r, equations (5)-(8) of Kanamori and Cipar (1974), except for the fact that in this study, the eigenfunctions of gravitational potential ${}_nP_l$ (or y_5 of a given n and l) replace the eigenfunctions of vertical displacement y_1 of Kanamori and Cipar (1974).

As stated earlier, equation (1) is formulated in a particular coordinate frame with the source at the polar axis. However, in geodesy, expansion of gravitational potential in terms of SH basis functions is conventionally formulated in the Earth-centered Earth-fixed (ECEF) frame with its z axis through the north pole and its x axis through the intersection of the Greenwich meridian and the equator. To rewrite equation (1) in the ECEF frame, the SH coefficients should be transformed from the original to the ECEF frame using the rotation angles based on geographic location of the earthquake point source. Transformation of SH coefficients under rotation is done using Wigner D-functions (e.g., Sneeuw, 1992; Wigner, 1959). In the ECEF frame, the geopotential coefficients beyond SH order $m = 2$ become non-zero and equation (1) is reformulated into

$$ \delta V(r,\theta,\lambda,t) = \frac{\mathrm{GM}}{a}\sum_{l=0}^{\infty}\left(\frac{a}{r}\right)^{l+1}\sum_{m=0}^{l}P_{lm}(\cos\theta)\{\Delta C_{lm}(t)\cos m\lambda + \Delta S_{lm}(t)\sin m\lambda\} \tag{6} $$

$$ \Delta C_{lm}(t) = \sum\nolimits_n \Delta C_{lm}\,{}_nf_l(t) \tag{7a} $$

$$ \Delta S_{lm}(t) = \sum\nolimits_n \Delta S_{lm}\,{}_nf_l(t) \tag{7b} $$

where ${}_n\Delta C_{lm}$ and ${}_n\Delta S_{lm}$ for each n, l and m are obtained by rotation of the five coefficients ${}_n\delta C_{l0}$,${}_n\delta C_{l1}$,${}_n\delta S_{l1}$, ${}_n\delta C_{l2}$, and ${}_n\delta S_{l2}$ given in equation (4); see Stein and Geller (1977) and Han et al. (2013) for details. Please refer to Chao and Gross (1987) for an alternative formulation of the normal mode summation of gravitational potential that does not make use of the coordinate frame rotation.

Equation (5) is evaluated using the eigenfunctions and their radial derivatives of the spheroidal modes, which can be pre-determined from an elastic Earth model. In this study, we use a spherically

Table 1
Spherical Harmonic Coefficients of Gravitational Potential Change Due to the ${}_0S_2$ and ${}_0S_3$ Spheroidal Modes, Along with Their Period (${}_nT_l$) in Minutes and Attenuation Factor (${}_nQ_l$).

${}_nS_l$	n	l	m	${}_n\Delta C_{lm}$	${}_n\Delta S_{lm}$	${}_nT_l$	${}_nQ_l$
${}_0S_2$	0	2	0	1.597×10^{-11}	0	53.895	509.682
${}_0S_2$	0	2	1	1.507×10^{-12}	-7.047×10^{-12}	53.895	509.682
${}_0S_2$	0	2	2	2.801×10^{-11}	3.936×10^{-12}	53.895	509.682
${}_0S_3$	0	3	0	3.685×10^{-12}	0	35.576	417.550
${}_0S_3$	0	3	1	-1.520×10^{-12}	1.161×10^{-11}	35.576	417.550
${}_0S_3$	0	3	2	5.386×10^{-12}	-2.898×10^{-12}	35.576	417.550
${}_0S_3$	0	3	3	-4.028×10^{-12}	1.641×10^{-11}	35.576	417.550

symmetric, nonrotating, elastic, and one-dimensional Earth model, namely, Preliminary Reference Earth Model (PREM; Dziewonski & Anderson, 1981). We use the publicly available software MINEOS (http://geodynamics.org/cig/software/mineos/), developed by Guy Masters (Masters et al., 2014; see also Gilbert & Backus, 1966, and Woodhouse, 1980) to compute the numerical tables of spheroidal modes of radial and lateral deformation and gravitational potential changes (${}_nU_l$, ${}_nV_l$, ${}_nP_l$) and their radial derivatives ($\frac{d_nU_l}{dr}$, $\frac{d_nV_l}{dr}$, and $\frac{d_nP_l}{dr}$) evaluated at different radii, along with their corresponding eigenfrequencies ${}_n\omega_l$ as well as attenuation factors ${}_nQ_l$. After normalizing the set of the MINEOS eigenfunctions to be suitable for use in equation (4), we compute the SH coefficients of gravitational potential change for each individual normal mode. Care must be taken not to use spheroidal modes computed with large uncertainties due to numerical problems. Details of MINEOS mode computation and its numerical stability can be found in Masters et al. (2014).

3. Seismic Perturbation in Surface Gravity

We computed the spheroidal normal modes for the degree l from 2 to 50 (wavelengths longer than 800 km), and for the period ${}_nT_l$ from ~54 min (associated with the so-called "football" mode ${}_0S_2$) down to 10 s. In total, about 120,000 modes were computed and a handful of them, particularly the high-frequency ones, are not numerically valid, and thus, not used.

As the first step, we evaluated the normal mode computation results by summing all valid modes in a brute force way to compute the "static" Green's functions of the geopotential at the Earth surface ($r = a$), $\sum_n K_l^0(r_s)\,{}_nP_l(a)$, $\sum_n K_l^1(r_s)\,{}_nP_l(a)$, and $\sum_n K_l^2(r_s)\,{}_nP_l(a)$, as in Han et al. (2013). These results are compared with the ones directly evaluated from the solutions of the equations of equilibrium of the deformed Earth (Piersanti et al., 1995; Pollitz, 1992; Smylie & Mansinha, 1971). Because the vertical deformation also plays a significant role in gravity change (Han et al., 2013), we do the comparison for the "static" Green's functions of the vertical deformation, $\sum_n K_l^0(r_s)\,{}_nU_l(a)$, $\sum_n K_l^1(r_s)\,{}_nU_l(a)$, and $\sum_n K_l^2(r_s)\,{}_nU_l(a)$, as well.

Figure S1 in the supporting information presents results of the comparison of the geopotential (top panels) and the vertical deformation (bottom panels) in terms of spectrum of the "static" Green's functions, for the case of the source with SH order $m = 0$, $m = 1$, and $m = 2$ at depth of 20 km ($r_s = a - 20$ km). Apart from the slight degradation in the case of vertical deformation for the case of $m = 0$ and $m = 1$, which is very likely due to numerical instability of individual mode computation, agreement between the normal mode summation and the equilibrium solution is satisfactory.

Using the double-couple solution from Stein and Okal (2005) for the 2004 Sumatra earthquake, SH coefficients of geopotential change due to individual normal modes were computed. Table 1 shows an example of the computed SH coefficients along with their periods and attenuation factors for the ${}_0S_2$ and ${}_0S_3$ spheroidal modes. Next, we evaluated temporal changes of geoid undulation δN and gravity disturbance δg using all modes up to 100 mHz (or 10 s in terms of period) and down to 800 km in wavelength as follows (Heiskanen & Moritz, 1967):

$$\delta N(\theta,\lambda,t) = a\sum_{l=2}^{50}\sum_{m=0}^{l} P_{lm}(\cos\theta)\{\Delta C_{lm}(t)\cos m\lambda + \Delta S_{lm}(t)\sin m\lambda\} \tag{8}$$

$$\delta g(\theta,\lambda,t) = \frac{GM}{a^2}\sum_{l=2}^{50}(l+1)\sum_{m=0}^{l} P_{lm}(\cos\theta)\{\Delta C_{lm}(t)\cos m\lambda + \Delta S_{lm}(t)\sin m\lambda\} \tag{9}$$

Figures 1a and 1b show the predicted transient changes in geoid undulation and gravity disturbance, respectively, evaluated every 15 min over the first couple of hours, and at 3, 6, 12, and 24 hr after the 2004 earthquake. The changes are as large as a few mm of geoid and several μGal (10^{-8} m/s^2) of gravity disturbance

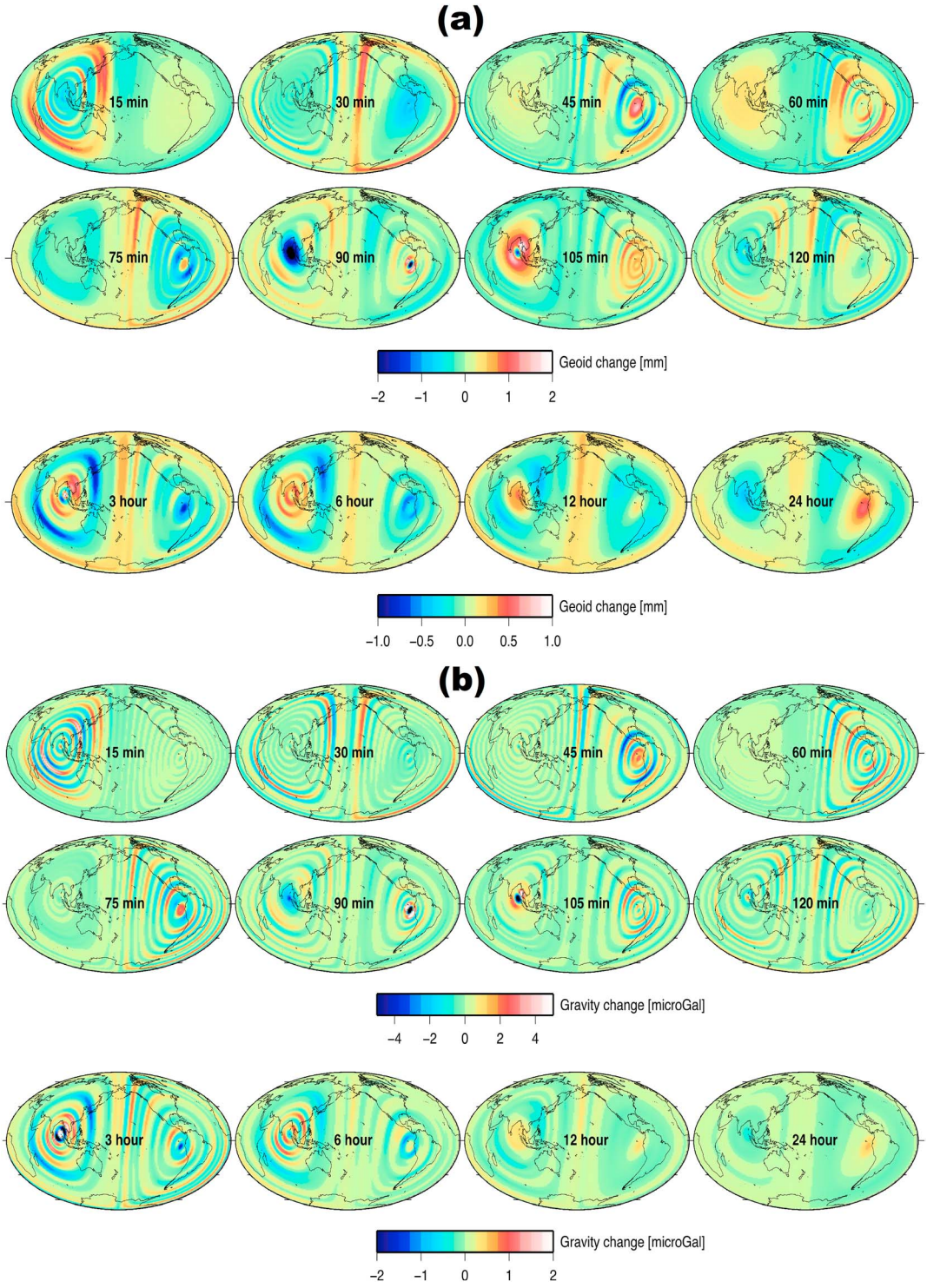

Figure 1. Transient oscillations of (a) geoid undulation and (b) gravity disturbance over the first 24 hr after the 2004 Sumatra earthquake, computed using normal mode summation of modes up to the frequency of 100 mHz and the spherical harmonic degree of 50. The 2004 Sumatra earthquake occurred at 00:58:53 UTC on 26 December, with an epicenter off the west coast of northern Sumatra. Each panel shows change at the indicated time after the earthquake rupture initiation.

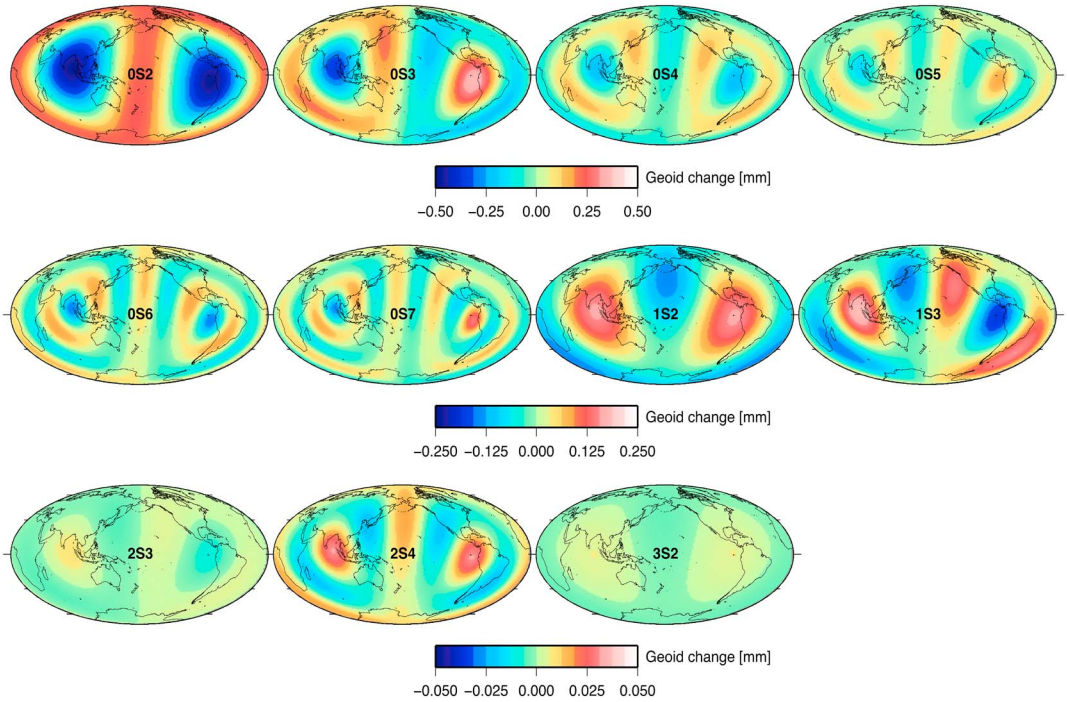

Figure 2. Geoid change due to the individual gravest spheroidal normal modes of the Earth excited by the 2004 Sumatra earthquake. The selected 11 gravest modes last longer than a day with the amplitude reduced only to 37% (e^{-1}) or less in a day. Each mode has different periods of oscillation including ~54 min for the ${}_0S_2$ mode.

during the first 2 hr. Oscillatory gravitational changes converge to the antipode of the earthquake epicenter to the west of Northern Peru roughly 45 min after the earthquake, which is incidentally comparable to the group time for the fastest overtone Rayleigh waves to reach the antipode. This figure also shows that most of the high-frequency modes disappear in the first 24 hr. It can also be seen that the strongest transient gravity changes occur at the epicenter of the earthquake and its antipode.

Although most of the spheroidal modes attenuate quickly and disappear in a couple of hours after the earthquake, there are 11 gravest modes with ~1 mHz or lower frequency that can last longer than a day with an amplitude decay of 37% (e^{-1}) or less in a day. These 11 modes along with their periods (in minutes) and attenuation factors are ${}_0S_2$ (${}_0T_2 \cong 54$, ${}_0Q_2 \cong 509$), ${}_0S_3$ (${}_0T_3 \cong 36$, ${}_0Q_3 \cong 418$), ${}_0S_4$ (${}_0T_4 \cong 26$, ${}_0Q_4 \cong 373$), ${}_0S_5$ (${}_0T_5 \cong 20$, ${}_0Q_5 \cong 355$), ${}_0S_6$ (${}_0T_6 \cong 16$, ${}_0Q_6 \cong 348$), ${}_0S_7$ (${}_0T_7 \cong 14$, ${}_0Q_7 \cong 342$), ${}_1S_2$ (${}_1T_2 \cong 25$, ${}_1Q_2 \cong 310$), ${}_1S_3$ (${}_1T_3 \cong 18$, ${}_1Q_3 \cong 283$), ${}_2S_3$ (${}_2T_3 \cong 13$, ${}_2Q_3 \cong 415$), ${}_2S_4$ (${}_2T_4 \cong 12$, ${}_2Q_4 \cong 380$), and ${}_3S_2$ (${}_3T_2 \cong 15$, ${}_3Q_2 \cong 365$). The spatial pattern of the geoid excitation by each of these gravest modes is presented in Figure 2. The gravest normal mode ${}_0S_2$, which is associated with the five SH degree 2 coefficients of $n = 0$ in equation (7), causes excitations of as large as 0.5 mm in the geoid. The largest perturbation is found equal around the epicenter and its antipode for all the modes.

The square root of degree variance of geoid change for the spheroidal modes with the overtone index of 0 (fundamental mode), 1, 2, and 3 were computed and compared with that of the GRACE monthly uncertainty in Figure 3. For GRACE, we used the calibrated uncertainty of December 2004 provided by the Release 5 solutions of the Center for Space Research (Bettadpur, 2012). It is found that the globally averaged magnitude of geoid excitation by the gravest modes, as characterized by degree variance, may be only a few times smaller than the uncertainty of monthly global GRACE geopotential data, in the case of ${}_0S_2$, ${}_0S_3$, ${}_0S_4$, ${}_1S_2$, ${}_1S_3$, and ${}_1S_4$. It is also seen that the spheroidal modes ${}_2S_l$ have the largest power between SH degree 6 and 13.

4. Seismic Perturbation in Orbital Trajectory

In this section, we examine earthquake-induced perturbations in inter-satellite ranging data as measured by two GRACE satellites. To be specific, we determine the frequencies at which the GRACE KBR signals are

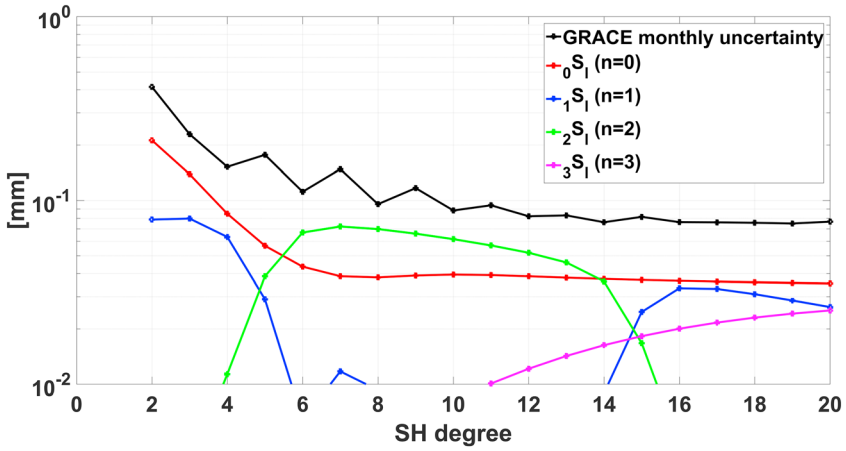

Figure 3. Square root of degree variance of geoid change computed from earthquake geopotential change coefficients ($_n\Delta C_{lm}$ and $_n\Delta S_{lm}$) of the spheroidal modes with overtone $n = 0$ (red), $n = 1$ (blue), $n = 2$ (green) and $n = 3$ (purple). For comparison, square root of degree variance of the GRACE monthly uncertainty of December 2004 from CSR Release 5 solutions is also shown (black).

excited due to gravity field variations induced by spheroidal oscillations of the Earth. The orbital perturbations caused by the periodic changes in the gravity field such as due to free oscillations are not as straightforward to understand as the time series of gravity changes on the Earth's surface, simply because satellites ("receivers" in this case) continuously orbit around the Earth. There must be coupling in the orbit perturbations between the period of the normal modes and the period of GRACE's motion around the rotating Earth. Cheng (2002) discussed a similar problem of perturbations in the GRACE KBR data, but caused by ocean tides.

Excitations in orbital trajectory are better understood using a formalism that treats satellite data as a time series along the orbit rather than as a function of the spatial coordinates (as in the spherical harmonics formalism by equation (6)). To that end, we use the Kaula representation of gravitational potential in orbital coordinates (Kaula, 1966). For a circular orbit with zero eccentricity, equations (6) and (7) can be reformulated into (Kaula, 1966):

$$\delta V(r,u,\Lambda,t) = \frac{GM}{a}\sum_{l=2}^{\infty}\left(\frac{a}{r}\right)^{l+1}\sum_{m=0}^{l}\sum_{k=-l}^{l}F_{lmk}(i)\{\alpha_{lm}(t)\cos\psi_{mk}(t)+\beta_{lm}(t)\sin\psi_{mk}(t)\} \tag{10}$$

$$\alpha_{lm}(t) = \begin{bmatrix}\Delta C_{lm}(t)\\ -\Delta S_{lm}(t)\end{bmatrix}_{l-m=\text{odd}}^{l-m=\text{even}} \tag{11a}$$

$$\beta_{lm}(t) = \begin{bmatrix}\Delta S_{lm}(t)\\ \Delta C_{lm}(t)\end{bmatrix}_{l-m=\text{odd}}^{l-m=\text{even}} \tag{11b}$$

where $F_{lmk}(i)$ is the inclination function, i is the orbit inclination, r is the distance of satellite from the Earth's center, u is the argument of latitude, and Λ is the longitude of the ascending node in the ECEF frame. The latter two are defined as $u(t) = \omega(t)+M(t)$ and $\Lambda(t) = \Omega(t) - \Theta(t)$, where ω is the argument of perigee (not to be confused with eigenfrequency of the normal modes), M is the mean anomaly, Ω is the right ascension of the ascending node, and Θ is the Greenwich sidereal time. We make use of the index k (which runs from $-l$ to l in steps of 2) in equation (10) instead of the p-index (which runs from 0 to l in unit steps) used by Kaula (1966). This is because the index k has the exact meaning of azimuthal order or SH order in the satellite frame (Sneeuw, 2000), and it is more appropriate for describing excited frequencies in the along-track observations. The angular argument $\psi_{mk}(t)$ is given by

$$\psi_{mk}(t) = ku(t) + m\Lambda(t) \tag{12}$$

Equation (10) explicitly represents the time series of the along-track gravitational potential perturbations as a function of the free oscillation forcing $\Delta C_{lm}(t)$ and $\Delta S_{lm}(t)$, and of the argument $\psi_{mk}(t)$. The free

oscillations are characterized by their own eigenfrequencies ${}_n\omega_l$, while the satellite is characterized by its basic frequencies $\dot{u}$ and $\dot{\Lambda}$. $\dot{u}$ and $\dot{\Lambda}$ are basic frequencies of a satellite in a nominal circular orbit with a constant radius r and inclination i. The nominal orbit is secularly precessing due primarily to the Earth's flattening J_2 ($=-\sqrt{5}\bar{C}_{20}$). The secular rates of u and Λ caused by J_2 are obtained as (Kaula, 1966; Sneeuw, 2000)

$$\dot{u} = \dot{\omega} + \dot{M} = n_0 + \frac{3}{2} n_0 J_2 \left(\frac{a}{r}\right)^2 \left[4\cos^2 i - 1\right] \tag{13}$$

$$\dot{\Lambda} = \dot{\Omega} - \dot{\Theta} = -\frac{3}{2} n_0 J_2 \left(\frac{a}{r}\right)^2 \cos i - \frac{2\pi}{\text{day}} \tag{14}$$

with n_0 being the mean motion of the satellite. For the GRACE orbit in December 2004 (with altitude of ~470 km and inclination of ~89°), we have $\dot{u} \cong 0.18$ mHz and $\dot{\Lambda} \cong -0.01$ mHz. In the case of GRACE, since $\dot{\Omega}$ is four orders of magnitude smaller than $\dot{\Theta}$, we sometimes refer to $\dot{\Lambda}$ as the Earth's rotation rate in the remainder of this paper. Now we examine the geopotential and orbit excitations by some of the gravest normal modes of the Earth.

4.1. Along-Track Excitations Due to the "Football" Mode ${}_0S_2$

We start with examining the excitations by the "football" mode, which is the longest-lasting one (except for the radial modes with $l = 0$, which are not considered in this study) and also generates the largest perturbations in surface gravity (see Figure 3). As described in section 2, coefficients ${}_0\Delta C_{2m}(t)$ and ${}_0\Delta S_{2m}(t)$ ($m = 0, 1,$ and 2) consist of two terms that describe (1) permanent (Heaviside step) changes represented by ${}_0\Delta C_{2m}$ and ${}_0\Delta S_{2m}$ and (2) transient changes represented by $-{}_0\Delta C_{2m}\cos({}_0\omega_2 t)\exp\left(\frac{-{}_0\omega_2 t}{2_0 Q_2}\right)$ and $-{}_0\Delta S_{2m}\cos({}_0\omega_2 t)\exp\left(\frac{-{}_0\omega_2 t}{2_0 Q_2}\right)$. As a result, we have two classes of excited frequencies: (1) those due to permanent changes in geopotential and (2) those due to transient changes. The second class incorporates eigenfrequencies of the normal modes. We refer to the first class as the "permanent excited frequencies" in the following, while the second class is simply called the excited frequencies.

First, we derive the "permanent excited frequencies" in geopotential due to the ${}_0S_2$ mode. Incorporating the static coefficients ${}_0\Delta C_{2m}$ and ${}_0\Delta S_{2m}$ in equation (10) results in

$$\begin{aligned}
\frac{GM}{a}\left(\frac{a}{r}\right)^3 \sum_{m=0}^{2}\sum_{k=-2}^{2} F_{lmp}(i)\left\{a_{lm}\cos\psi_{lmp}(t) + \beta_{lm}\sin\psi_{lmp}(t)\psi\right\} = \frac{GM}{a}\left(\frac{a}{r}\right)^3 \times \\
\left[F_{2,0,1}(i)\,{}_0\Delta C_{2,0}\right. \\
+\left\{F_{2,0,0}(i) + F_{2,0,2}(i)\right\}{}_0\Delta C_{2,0}\ \cos(2\dot{u}t) \\
-F_{2,1,0}(i)\,{}_0\Delta S_{2,1}\cos\left((2\dot{u}+\dot{\Lambda})t\right) + F_{2,1,0}(i)\,{}_0\Delta C_{2,1}\sin\left((2\dot{u}+\dot{\Lambda})t\right) \\
-F_{2,1,1}(i)\,{}_0\Delta S_{2,1}\ \cos(\dot{\Lambda}t) + F_{2,1,1}(i)\,{}_0\Delta C_{2,1}\sin(\dot{\Lambda}t) \\
-F_{2,1,2}(i)\,{}_0\Delta S_{2,1}\cos\left((-2\dot{u}+\dot{\Lambda})t\right) + F_{2,1,2}(i)\,{}_0\Delta C_{2,1}\sin\left((-2\dot{u}+\dot{\Lambda})t\right) \\
+F_{2,2,0}(i)\,{}_0\Delta C_{2,2}\cos\left((-2\dot{u}+2\dot{\Lambda})t\right) + F_{2,2,0}(i)\,{}_0\Delta S_{2,2}\sin\left((2\dot{u}+2\dot{\Lambda})t\right) \\
+F_{2,2,1}(i)\,{}_0\Delta C_{2,2}\cos(2\dot{\Lambda}t) + F_{2,2,1}(i)\,{}_0\Delta S_{2,2}\sin(2\dot{\Lambda}t) \\
\left.+F_{2,2,2}(i)\,{}_0\Delta C_{2,2}\cos\left((-2\dot{u}+2\dot{\Lambda})t\right) + F_{2,2,2}(i)\,{}_0\Delta S_{2,2}\sin\left((-2\dot{u}+2\dot{\Lambda})t\right)\right]
\end{aligned} \tag{15}$$

Equation (15) shows that in total seven distinct frequencies are excited due to static part of the ${}_0S_2$ mode. They are $\dot{\Lambda}$, $2\dot{\Lambda}$, $2\dot{u}$, $2\dot{u}\pm\dot{\Lambda}$, and $2\dot{u}\pm2\dot{\Lambda}$. Among them, $\dot{\Lambda}$ (approximately once per day) and $2\dot{\Lambda}$ (approximately twice per day) are below 1 cycle-per-revolution (CPR). In this study, we focus on the transient changes associated with the normal modes. For further discussion on permanent changes in the inter-satellite range perturbation after earthquakes, see Han et al. (2010, 2011).

As the next step, we derive the excited frequencies due to the transient gravitational potential change with the eigenfrequency of ~0.31 mHz (~54 min) associated with the ${}_0S_2$ mode. Substituting $\alpha_{lm}(t)$ and $\beta_{lm}(t)$ from equations (7) and (11) into equation (10) gives the potential excitation as

$$\frac{GM}{a}\left(\frac{a}{r}\right)^3\sum_{m=0}^{2}\sum_{k=-2}^{2}F_{lmp}(i)\left\{a_{lmp}(t)\cos\psi_{lmp}(t)+\beta_{lm}(t)\sin\psi_{lmp}(t)\right\}=\frac{GM}{a}\left(\frac{a}{r}\right)^3\times \tag{16}$$

$$\begin{aligned}
&\Big[-\frac{1}{2}{}_0Z_2\left\{F_{2,0,0}(i)+F_{2,0,2}(i)+F_{2,0,2}(i)\right\}{}_0\Delta C_{2,0}\cos(({}_0\omega_2-2\dot{u})t)\\
&+\frac{1}{2}{}_0Z_2F_{2,1,0}(i){}_0\Delta S_{2,1}\cos\left(({}_0\omega_2-2\dot{u}-\dot{\Lambda})t\right)+\frac{1}{2}{}_0Z_2F_{2,1,0}(i){}_0\Delta C_{2,1}\sin\left(({}_0\omega_2-2\dot{u}-\dot{\Lambda})t\right)\\
&+\frac{1}{2}{}_0Z_2F_{2,1,2}(i){}_0\Delta S_{2,1}\cos\left(({}_0\omega_2-2\dot{u}+\dot{\Lambda})t\right)-\frac{1}{2}{}_0Z_2F_{2,1,2}(i){}_0\Delta C_{2,1}\sin\left(({}_0\omega_2-2\dot{u}+\dot{\Lambda})t\right)\\
&-\frac{1}{2}{}_0Z_2F_{2,2,0}(i){}_0\Delta C_{2,2}\cos\left(({}_0\omega_2-2\dot{u}-\dot{\Lambda})t\right)+\frac{1}{2}{}_0Z_2F_{2,2,0}(i){}_0\Delta S_{2,2}\sin\left(({}_0\omega_2-2\dot{u}-2\dot{\Lambda})t\right)\\
&-\frac{1}{2}{}_0Z_2F_{2,2,2}(i){}_0\Delta C_{2,2}\cos\left(({}_0\omega_2-2\dot{u}+\dot{\Lambda})t\right)-\frac{1}{2}{}_0Z_2F_{2,2,2}(i){}_0\Delta S_{2,2}\sin\left(({}_0\omega_2-2\dot{u}+2\dot{\Lambda})t\right)\\
&+\text{higher frequency terms}\Big]
\end{aligned}$$

where ${}_0Z_2=\exp\left(\frac{-{}_0\omega_2 t}{2{}_0Q_2}\right)$. The first nine terms in equation (16) represent five excited frequencies grouped around ${}_0\omega_2-2\dot{u}$. Similarly, the "higher frequency terms" (higher than 1 CPR), which are not explicitly shown, include excited frequencies grouped around ${}_0\omega_2$ and ${}_0\omega_2+2\dot{u}$. They are listed as

$$\left({}_0\omega_2-2\dot{\Lambda}\right),\left({}_0\omega_2-\dot{\Lambda}\right),{}_0\omega_2,\left({}_0\omega_2+\dot{\Lambda}\right),\text{and }\left({}_0\omega_2+2\dot{\Lambda}\right) \tag{17}$$

$$\left({}_0\omega_2+2\dot{u}-2\dot{\Lambda}\right),\left({}_0\omega_2+2\dot{u}-\dot{\Lambda}\right),\left({}_0\omega_2+2\dot{u}\right),\left({}_0\omega_2+2\dot{u}+\dot{\Lambda}\right),\text{and }\left({}_0\omega_2+2\dot{u}+2\dot{\Lambda}\right) \tag{18}$$

Equation (16) represents a Fourier series with a finite set of excited frequencies. It shows that the ${}_0S_2$ mode excites geopotential changes along the satellite trajectory at 15 distinct frequencies. These 15 frequencies are the result of linear combination of the satellite angular velocity in the orbital plane $\dot{u}$ (~0.18 mHz), the Earth's rotation rate $\dot{\Lambda}$ (~−0.01 mHz), and the normal mode eigenfrequency ${}_0\omega_2$ (~0.31 mHz). Note that since $\dot{\Lambda}$ is considerably smaller than $\dot{u}$ and ${}_0\omega_2$, the 15 excited frequencies appear around three distinct frequencies of ${}_0\omega_2-2\dot{u}$ (~0.05 mHz), ${}_0\omega_2$ (~0.31 mHz), and ${}_0\omega_2+2\dot{u}$ (~0.67 mHz). Note that this "splitting" of the mode ${}_0S_2$ into three groups of five singlets is 1 order of magnitude coarser than the splitting due to rotation and ellipticity, traditionally observed in seismology (Benioff et al., 1961; Ness et al., 1961), whose range does not exceed ± 0.01 mHz (Okal & Stein, 2009). In this context, it does not seem necessary to include the rotational and elliptical splitting of the Earth's modes in the present computation.

Thus far, we discussed the excitations in geopotential changes along the orbit, whereas GRACE observes orbit perturbations as in inter-satellite range or range-rate. Nevertheless, it is well known (e.g., Sneeuw, 2000) that a perturbing potential (or force) with a certain frequency causes perturbation in the orbital trajectory at the same frequency. This is simply because orbit perturbations are obtained by linear perturbation theory, either using the Lagrange planetary equations (e.g., Kaula, 1966; Rosborough, 1986) or the Hill equations (e.g., Schrama, 1989; Sneeuw, 2000), and in any linear dynamic system, the input and output frequencies are the same. As such, the GRACE range-rate perturbations due to Earth's free oscillations could be formulated using an equation of the following form:

$$\delta\dot{\rho}(r,u,\Lambda,t)=\sum_{l=2}^{\infty}\sum_{m=0}^{l}\sum_{k=-l}^{l}H_{lmk}^{\delta\dot{\rho}}\left\{\alpha'_{lm}(t)\cos\psi_{mk}(t)+\beta'_{lm}(t)\sin\psi_{mk}(t)\right\} \tag{19}$$

$$\alpha'_{lm}(t)=\begin{bmatrix}\Delta C_{lm}(t)\\ \Delta S_{lm}(t)\end{bmatrix}_{l-m=\text{odd}}^{l-m=\text{even}} \tag{20a}$$

$$\beta'_{lm}(t)=\begin{bmatrix}-\Delta S_{lm}(t)\\ \Delta C_{lm}(t)\end{bmatrix}_{l-m=\text{odd}}^{l-m=\text{even}} \tag{20b}$$

where $H_{lmp}^{\delta\dot{\rho}}$ is the *linear* transfer function that maps the along-track gravitational potential changes to range-

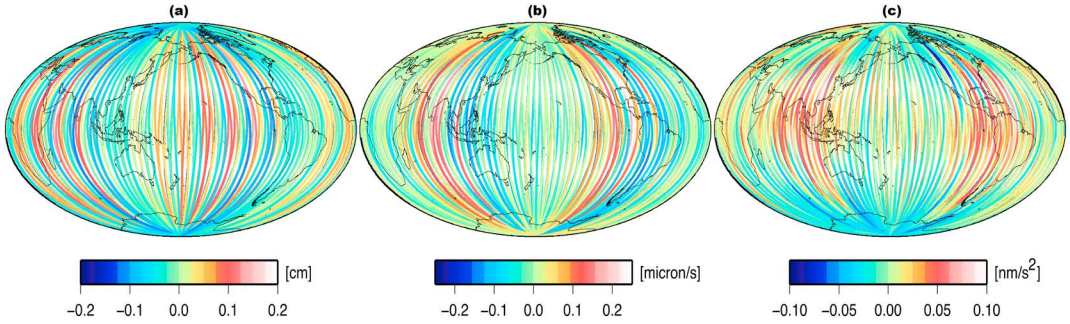

Figure 4. Synthetic GRACE orbit perturbations in terms of inter-satellite (a) range, (b) range-rate, and (c) range-acceleration caused by the gravitational potential change associated with the ${}_0S_2$ mode. Results are computed using numerical orbit integration based on 6 days of synthetic data after the 2004 Sumatra earthquake.

rate perturbations in the spectral domain (see equation (3) of Wagner et al., 2006; for details, please also refer to Wagner, 1987; Kim, 2000; Sneeuw, 2000; Cheng, 2002; Visser, 2005).

We used numerical orbit integration to compute synthetic GRACE inter-satellite ranging perturbations due to the ${}_0S_2$ mode. To that end, reference orbits of the GRACE satellites are numerically integrated based on a static gravity field of the Earth. Then, the time-variable geopotential of SH degree-2 coefficients associated with the ${}_0S_2$ mode (see Table 1) are computed following equations (7) and (3), and added to the static gravity field to compute the perturbed orbits. Finally, perturbations in the inter-satellite ranging data are computed as the difference between the reference and perturbed orbits. Figure 4 shows the calculated perturbations in range, range-rate and range-acceleration along the actual GRACE ground tracks for 6 days after the 2004 Sumatra earthquake. The altitude of the satellites is around 470 km in December 2004. Changes of ~2 mm, ~0.2 μm/s, and ~0.1 nm/s^2, respectively, in inter-satellite range, range-rate, and range-acceleration are found over the ~220 km baseline.

Figure 5 presents the time series of the synthetic range and range-rate perturbations and the power spectral density (PSD) of the range-rate time series. The results of numerical integration validate the excited frequencies predicted by our analytic derivation based on the Kaula theory. Peak-to-peak variations in the range-rate time series reach ~0.5 μm/s. It is seen that due to the slow attenuation of ${}_0S_2$, the perturbations remain as significant as half of the initial perturbations even 6 days after the rupture. As predicted, a total of 15 frequencies, found at three distinct frequency bands, excited by the ${}_0S_2$ mode are clearly identified. The PSD shows that the large perturbations are found at the five lowest frequencies below 1 CPR (~0.18 mHz), with the largest one at ${}_0\omega_2 - 2\dot{u} - 2\dot{\Lambda}$ (~0.022 mHz) and the second largest at ${}_0\omega_2 - 2\dot{u}$ (~0.045 mHz); see also Figure 6.

In addition to the five excited frequencies ${}_0\omega_2 \pm m\,\dot{\Lambda}\,(m = 0, 1, 2)$ right below the 2 CPR frequency, the other range-rate perturbations found near 2 CPR are associated with the "permanent excited frequencies" $2\dot{u} \pm m\dot{\Lambda}$. The "permanent excited frequency" at $\dot{\Lambda}$ should have a negligible amplitude, since $F_{2,1,0}(i) \cong 0$ for polar or near polar orbits such as GRACE.

The free oscillation produces a transient gravitational perturbation that attenuates over time. The 1-D frequency analysis based on the Fourier transform does not provide any information about the signal attenuation. As such, it does not deliver an accurate picture of the phenomena under investigation. The 2-D time-frequency representation, on the other hand, shows how nonstationary signals evolve as a function of time. Therefore, it could serve as a more suitable tool for detection of transient signals. We applied the continuous wavelet transform approach (e.g., Keller, 2004) to obtain the 2-D time-frequency representation of the range-rate time series data. As the mother wavelet, the analytic Morse wavelet (Olhede & Walden, 2002) was chosen to generate the 2-D time-frequency map, known also as *spectrogram*. It should be noted that in wavelet analysis, the trade-off between temporal and frequency resolutions affects the amplitude of the generated 2-D time-frequency map (e.g., Chao et al., 2014). Thus, the employed wavelet analysis in this paper is mainly used for detection of the free oscillations rather than quantification of the amplitudes.

To give a clear picture of non-stationarity of free oscillations, we focus on the excited frequencies <1 CPR with larger amplitudes and more distinct frequencies. Figure 6a shows PSD of the synthetic range-rate

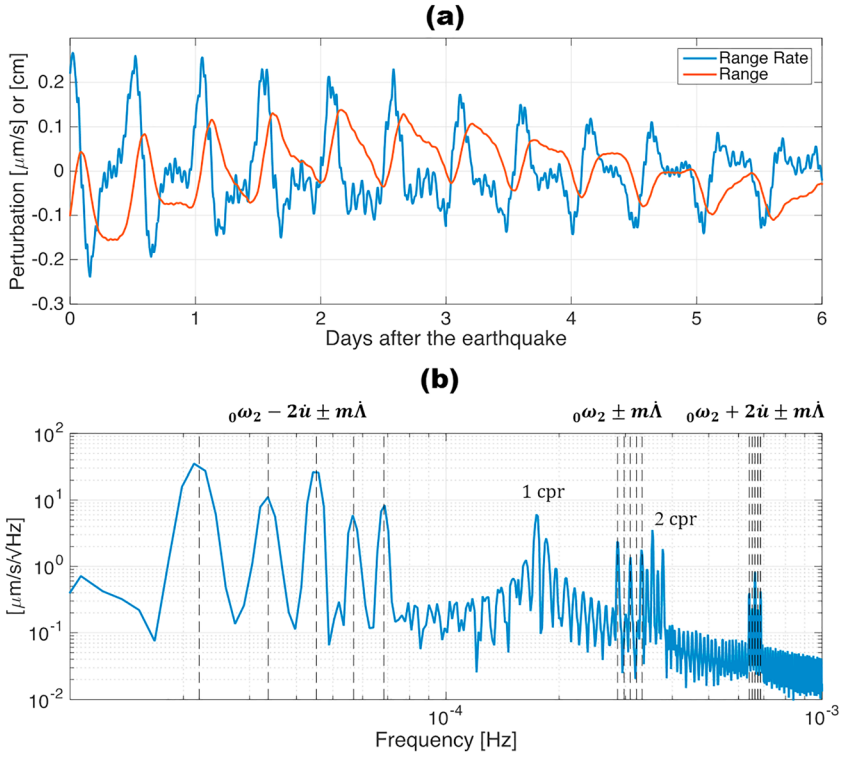

Figure 5. (a) Time-series of synthetic GRACE inter-satellite range (red) and range-rate (blue) perturbations due to the $_0S_2$ mode based on 6 days of data after the 2004 Sumatra earthquake, and (b) the corresponding power spectral density of the range-rate perturbations. The vertical dashed black lines indicate the excited frequencies predicted by the Kaula orbit perturbation theory. There are 15 distinct frequencies excited by the $_0S_2$ mode via coupling of the eigenfrequency ($_0\omega_2$), GRACE orbital frequency ($\dot{u}$), and Earth rotation rate ($\dot{\Lambda}$). Other excitations near 2 cycle-per-revolution are due to the permanent gravitational changes after the earthquake.

data due to the $_0S_2$ mode (as in Figure 5) for lower frequencies with the five excited frequencies indicated. The 2-D time-frequency map was generated based on the synthetic data from 21 to 31 of December 2004 and is shown in Figure 6b. As opposed to Figure 6a, wavelet analysis provides information about the starting time of the transient signal and its attenuation pattern. For example, it can be seen that the magnitude of range-rate perturbation at the frequency of $_0\omega_2 - 2\dot{u} - 2\dot{\Lambda}$ reaches 50% of its initial value 6 days after the earthquake, which mirrors the decay of the mode $_0S_2$, rather than that of the perturbation at its shifted frequency. It should be mentioned that the PSD of range-rate data shows five peaks at the frequency band below 0.1 mHz, while in the 2-D time-frequency map only two peaks, corresponding to the largest and second largest amplitudes in Figure 6a, are visible. This is simply due to the color scale used in Figure 6b.

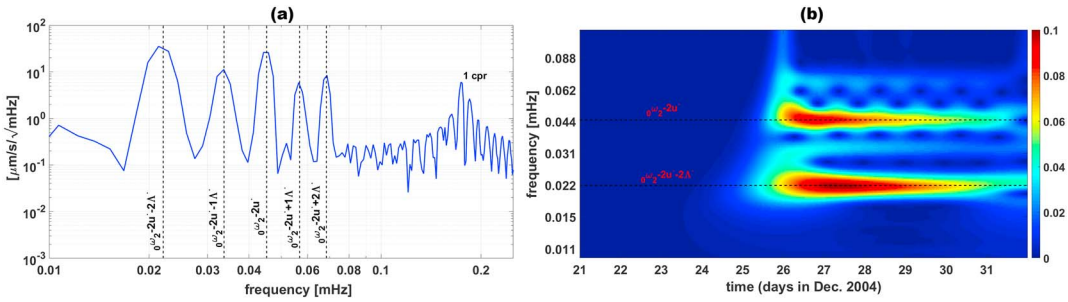

Figure 6. (a) Power spectral density of the synthetic GRACE range-rate perturbations due to the $_0S_2$ mode focused at lower frequencies, and (b) 2-D time-frequency map of the synthetic range-rate data from 21 to 31 December 2004 obtained using the wavelet analysis.

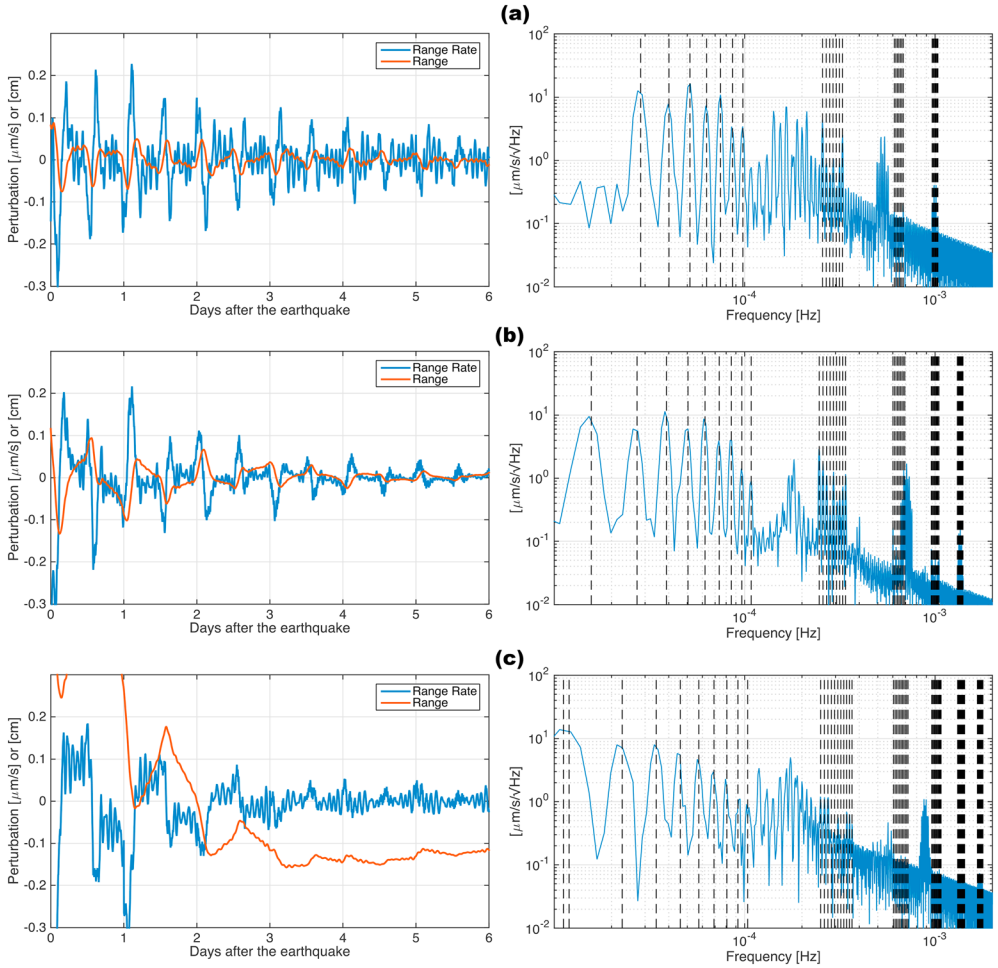

Figure 7. Same as Figure 5 but for the case of (a) ${}_0S_3$, (b) ${}_0S_4$ and (c) ${}_0S_5$ modes. The left and right panels show the time series and power spectral density, respectively. The vertical dashed lines are the frequencies predicted by the Kaula theory.

4.2. Along-Track Excitations Due to Other Gravest Modes

Using a similar procedure to the case of the ${}_0S_2$ mode, it can be shown that the Kaula linear perturbation theory predicts excitations by the spheroidal mode ${}_nS_l$ at the following frequencies:

$$\dot{\psi}_{mk}^{\ {}_n\omega_l} = \left|{}_n\omega_l + k\dot{u} \pm m\dot{\Lambda}\right| \tag{21}$$

where $-l \le k[2] \le l$ and $0 \le m \le l$. Note that "[2]" used with the index k indicates that it runs with steps of 2. The total number of excited frequencies by the ${}_nS_l$ mode is therefore $(2l+1) \times (l+1)$. For example, the ${}_0S_3$ mode excites the following 28 frequencies: $\left|{}_0\omega_3 - 3\dot{u} \pm m\dot{\Lambda}\right|$, $\left|{}_0\omega_3 - \dot{u} \pm m\dot{\Lambda}\right|$, $\left|{}_0\omega_3 + \dot{u} \pm m\dot{\Lambda}\right|$, and $\left|{}_0\omega_3 + 3\dot{u} \pm m\dot{\Lambda}\right|$ for $m = 0$, 1, 2 and 3. It is seen that they are grouped around the main four frequencies of $({}_0\omega_3 - 3\dot{u})$, $({}_0\omega_3 - \dot{u})$, $({}_0\omega_3 + \dot{u})$, and $({}_0\omega_3 + 3\dot{u})$.

Figure 7 illustrates other examples of synthetic range and range-rate perturbations computed using numerical orbit integration and the corresponding PSDs along with the excited frequency predicted from the Kaula theory, for the fundamental spheroidal modes of ${}_0S_3$, ${}_0S_4$, and ${}_0S_5$. The time series show that these three modes attenuate faster than ${}_0S_2$. Similar to ${}_0S_2$, most of the largest amplitudes occur at lower frequencies below 1 CPR. Figure 8 shows the examples of the higher overtone ($n > 0$) spheroidal modes ${}_1S_2$, ${}_1S_3$, and ${}_2S_4$ with a few days of decay time. Compared to the fundamental modes, perturbations are at least one order of magnitude smaller. Furthermore, all the excited frequencies happen to be above 1 CPR.

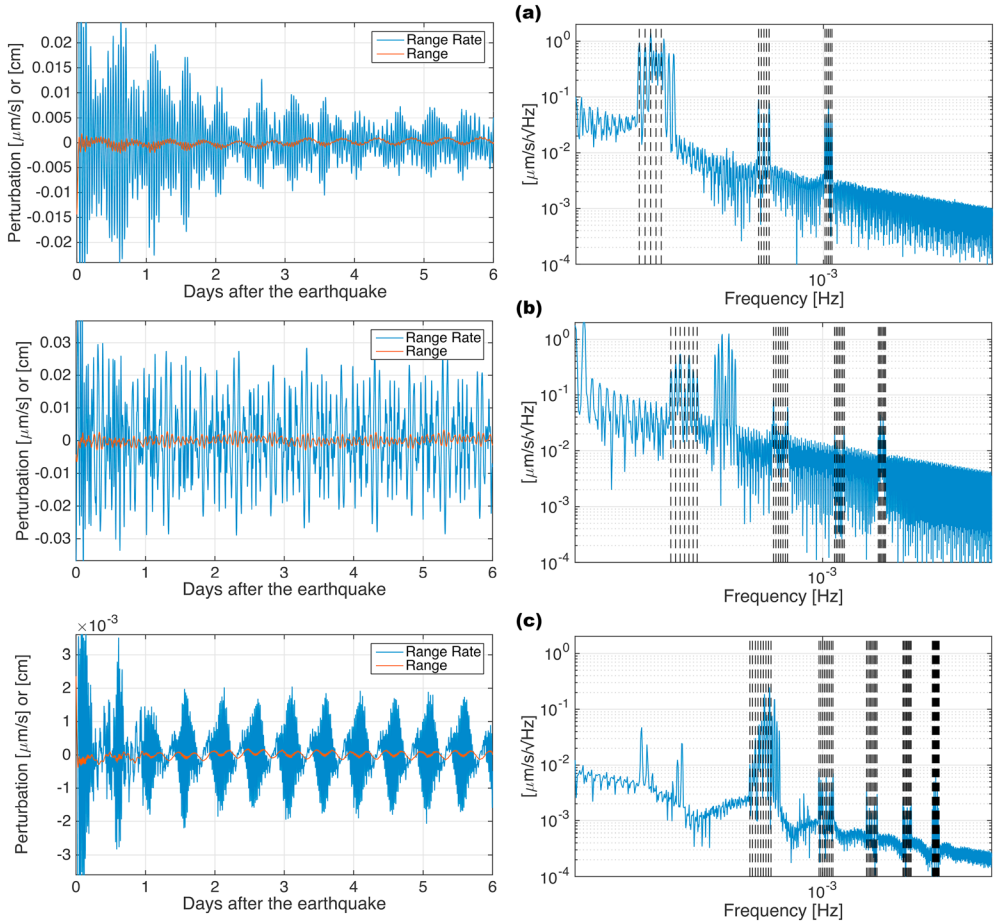

Figure 8. Same as Figure 7 but for the case of (a) ${}_1S_2$, (b) ${}_1S_3$, and (c) ${}_2S_4$ modes. All the excited frequencies by these modes happen to be above 1 cycle-per-revolution.

4.3. Comparison of Along-Track Excitations With the GRACE Measurement Error

We compared the range-rate perturbations with the actual KBR error to see if along-track excitations due to the gravest normal modes could be detected by GRACE. To that end, a realistic representation of the actual error of KBR data provided by Mayer-Gürr et al. (2018) is used. Using a simulation study, Mayer-Gürr et al. (2018) showed that accelerometer and KBR noise dominate the GRACE actual error budget at low and high frequencies, respectively, while the errors in atmosphere and ocean de-aliasing L1B (AOD1B) and geophysical background models (such as ocean tides), known as the temporal aliasing error, are the main source in the mid-frequency band. To be specific, the KBR and accelerometer instrument noise given by Kim (2000) fits the GRACE actual error at frequencies above ~10 mHz and below ~0.44 mHz, respectively. The temporal aliasing error given by Dobslaw et al. (2016) represents the GRACE actual error in the frequency band of 0.44–10 mHz. It is worth mentioning that Flury et al. (2008) showed that when the on-board heaters were deactivated, the GRACE accelerometers achieved the expected accuracy given by Kim (2000).

Figure 9 shows the synthetic KBR perturbations due to the ${}_0S_2$ mode, compared with the temporal aliasing error and accelerometer noise in terms of inter-satellite range-rate for frequencies below 10 mHz. It is seen that ${}_0S_2$ generates perturbations that are comparable to or only a few times smaller than the GRACE error at most of the excited frequencies. The results of comparison for the other gravest normal modes, namely, ${}_0S_3$, ${}_0S_4$, ${}_0S_5$, ${}_1S_2$, ${}_1S_3$, and ${}_2S_4$, are shown in Figures S2 to S7. We extended our analysis by finding the significant excited frequencies with peaks larger or less than 3 times smaller than the GRACE error; a total of 45 frequencies are identified as reported in Table S1 in the supporting information. Almost all of them have their frequencies below 1 mHz (~5 CPR). The gravest modes do not generate significant excitations at frequencies above 1 mHz.

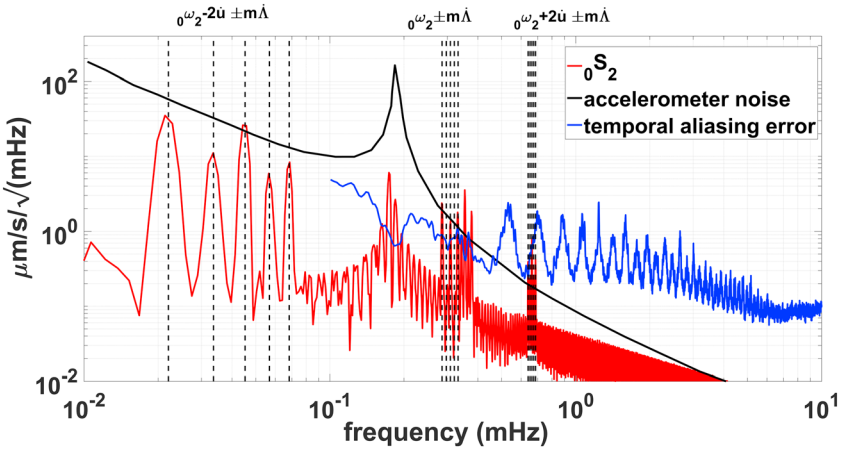

Figure 9. Comparison of synthetic GRACE range-rate perturbations due to the ${}_0S_2$ mode (red) with the actual GRACE K-band ranging error. The K-band ranging error budget is dominated by the accelerometer noise (black) at low frequencies below ~0.44 mHz and the temporal aliasing error (blue) at the frequency band between ~0.44 and 10 mHz. The low frequency perturbation by the ${}_0S_2$ mode is very likely to be contaminated by the GRACE accelerometer noise.

We primarily focus on the frequency band below 1 CPR to detect any transient gravitational change by free oscillation, because (1) numerous frequencies are excited within the frequency band of 1–5 CPR due to various spheroidal modes, and thus, it will be difficult to distinguish one from the other; (2) only the fundamental spheroidal modes ($n = 0$) cause excitations in range-rate below 1 CPR (that is why only 9 out of the 45 significant frequencies listed in Table S1 happen to be below 1 CPR); and (3) the excited frequencies below 1 CPR are most distinct. In particular, we first look for the two frequencies of ${}_0\omega_2 - 2\dot{u} - 2\dot{\Lambda}$ (~0.022 mHz) and ${}_0\omega_2 - 2\dot{u}$ (~0.045 mHz) excited by the spheroidal mode ${}_0S_2$. These two are supposed to have the largest and second largest amplitudes, respectively, among all others.

5. Did GRACE Detect the Earth's Free Oscillations Excited by the 2004 Sumatra Earthquake?

We examined the KBR (post-fit) range-rate residual data from GRACE in December 2004 to search for transient gravitational excitation of the free oscillations after the 2004 Sumatra earthquake (Park et al., 2005; Stein & Okal, 2005). The reference orbits used to compute the range-rate residual data are obtained using a data processing strategy similar to the one adopted by the ITSG-Grace2016 gravity field solutions (Mayer-Gürr et al., 2016). Various force models such as the geopotential model GOCO05S (Mayer-Gürr et al., 2015), high-frequency atmosphere and non-tidal ocean mass variability model AOD1B (Dobslaw et al., 2013), and ocean tides model EOT11a (Savcenko & Bosch, 2012), along with the ITSG-Grace2016 monthly mean solution of December 2004 and nongravitational accelerometer data, are used in numerical integration to calculate the reference orbits on a daily basis. The post-fit range-rate residuals are computed as the difference between the measured range-rate data and those computed from the reference orbits. Please note that coseismic gravity signal is not removed from the residual KBR data after the earthquake so that the synthetic and actual data analyses are fully consistent.

The non-gravitational accelerations measured by the GRACE on-board accelerometers are subject to instrument specific biases and scale factors (Bettadpur, 2009). The conventional approach for calibration of the accelerometer data is to estimate biases and scale factors on a daily basis. The ITSG-Grace2016 solutions employ an alternative approach, which models the variations in the biases every 6 hr using uniform cubic basis splines (Klinger & Mayer-Gürr, 2016). The approach based on the 6-hourly cubic splines may interfere with the low-frequency signals below 1 CPR in the KBR residual data, and therefore, it can distort the free oscillation signal (of our interest) in this frequency band. We computed two sets of post-fit residual KBR data using both the conventional and the 6-hourly cubic splines approaches. In the case of excited frequencies below 1 CPR, we exploited the KBR data obtained using the conventional method, whereas both sets of KBR data were analyzed to search for the excited frequencies above 1 CPR.

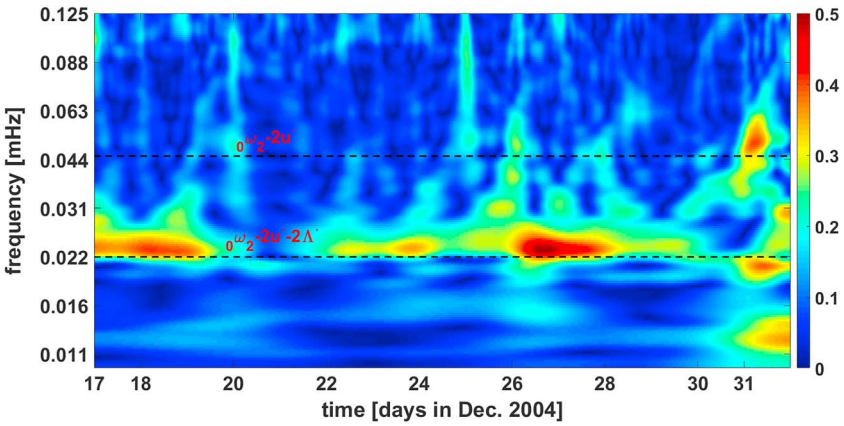

Figure 10. 2-D time-frequency map of the actual GRACE (post-fit) range-rate residual data from 17 to 31 December 2004 (shown for frequencies below 0.125 mHz). A strong transient signal appears in the GRACE data after the rupture on 26 December with a frequency of ~0.022 mHz, which could be associated with the largest excitation due to the ${}_0S_2$ mode.

We applied wavelet analysis to the post-fit range-rate residual data from 17 to 31 December 2004 obtained by the conventional accelerometer data calibration method. Figure 10 shows the 2-D time-frequency map for frequencies below 1 CPR. The gravitational free oscillation signals should occur after the earthquake rupture (at 00:58:53 UTC on 26 December 2004), coincide with the predicted excited frequencies, and attenuate over time. It can be seen that the 2-D time-frequency map indicates the emergence of such a transient signal on 26 December right after the rupture with a frequency, which is very close to the largest excitation due to the ${}_0S_2$ mode, namely, ${}_0\omega_2 - 2\dot{u} - 2\dot{\Lambda}$ (~ 0.022 mHz). The transient signal appears to last for 3 to 4 days after the earthquake in the GRACE KBR residual data. All of these indicate that it may be a possible signature of the gravitational changes associated with the Earth's free oscillations excited by the great 2004 Sumatra earthquake.

However, there is also inconsistency found between the GRACE KBR data and the synthetic range-rate: (1) the amplitude of the range-rate excitation is a few times larger than the one obtained from the synthetic data analysis (Figure 6); (2) although two times smaller, a gravitational excitation at the higher frequency of ~0.045 mHz (roughly four times per day) is predicted from the double-couple source, but not apparent in the GRACE data; and (3) the GRACE KBR data before the earthquake, especially from 17 to 19 December, seem to show anomalies at a similar frequency of ~0.022 mHz (roughly twice per day). However, these anomalies found before the earthquake grow (do not attenuate) over time, and thus, they can be discriminated from transient signals associated with the free oscillations.

We examined a possible contamination caused by the ocean tide model errors at the excited frequency of 0.022 mHz. We tested the ocean tides models FES2014 (Carrère et al., 2015) and EOT08ag, which uses tidal corrections obtained from several years of GRACE data (Mayer-Gürr et al., 2012). We also changed the arc length of orbit integration from 1 to 2 and 3 days to see the effect of different orbit parametrizations. Such modification in background ocean tidal models and arc lengths did not result in any notable difference from the one presented in Figure 10 (thus, not shown).

We also analyzed the KBR residual data in the time domain by comparing three days of data before and after the rupture to see if GRACE captured any identifiable change after the earthquake due to free oscillations. We applied least-squares harmonic analysis (e.g., Wells et al., 1985) using the five excited frequencies (below 1 CPR) of the ${}_0S_2$ mode, namely, ${}_0\omega_2 - 2\dot{u} \pm m\dot{\Lambda}$ with $m = 0$, 1, and 2. Figure 11 shows the results in terms of time series and PSD of the actual KBR data and those obtained from the least-squares fit. As opposed to the data before the earthquake, time series of the (smoothed) actual KBR residual data after the earthquake present a decaying pattern. Moreover, comparison of the results in terms of PSD shows that the harmonic analysis provides a better fit to the GRACE KBR data at the frequency of ${}_0\omega_2 - 2\dot{u} - 2\dot{\Lambda}$ after the earthquake (compare Figure 11b with Figure 11d), which is in agreement with the wavelet analysis. The harmonic fit of the ${}_0S_2$ mode to the GRACE data (blue curve in Figure 11) agrees better with its synthesis (red curve) after the earthquake, particularly in phase. Again, the amplitude of the observed excitations is larger than the one based on the synthesis with the point source double-couple solution by Stein and Okal (2005).

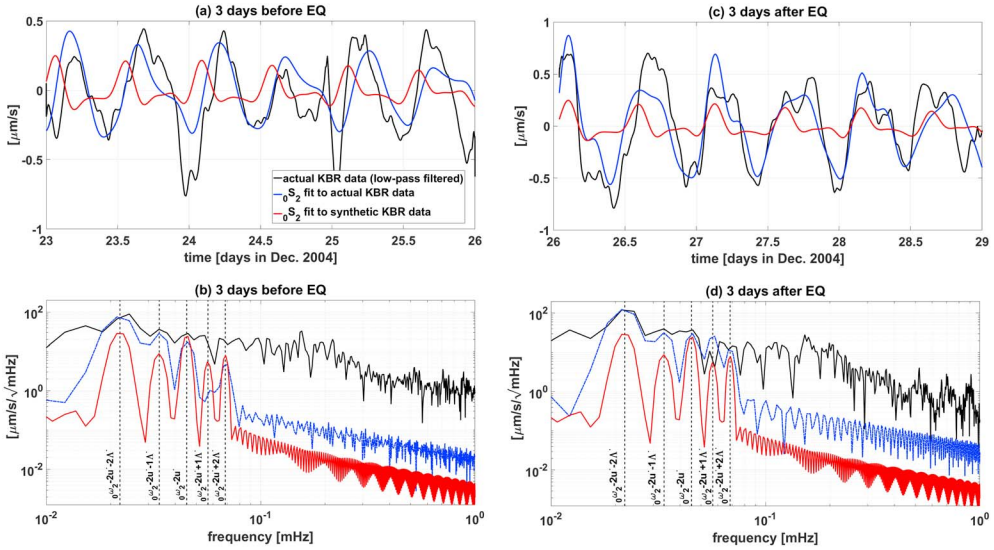

Figure 11. Comparison of the GRACE post-fit range-rate residual data for (a and b) 3 days before and (c and d) 3 days after the 2004 Sumatra earthquake: (a) Based on 3 days of data before the earthquake, this panel shows time series of the low-pass filtered GRACE K-band ranging (KBR) data with cut-off frequency at 1 CPR in *black*, the harmonic fit using the five excited frequencies ${}_0\omega_2 - 2\dot{u} \pm m\dot{\Lambda}$ ($m = 0$, 1 and 2) of the ${}_0S_2$ mode applied to the actual KBR data in *blue*, and the same harmonic fit applied to the synthetic KBR perturbations due to the ${}_0S_2$ mode in *red*. (b) Based on 3 days of data before the earthquake, this panel shows power spectral density of the actual KBR data in *black*, the harmonic fit to the actual KBR data in *blue*, and the harmonic fit to the synthetic KBR perturbations due to the ${}_0S_2$ mode in *red*. (c) Same as (a) but based on 3 days of data after the earthquake. (d) Same as (b) but based on 3 days of data after the earthquake. As opposed to the data before the earthquake, time series of the GRACE data after the earthquake present a decaying pattern, and also shows that the harmonic analysis better fits the GRACE KBR data. Most interestingly, the harmonic fit of the ${}_0S_2$ mode to the GRACE data agree better with its synthesis (red curve) after the earthquake, particularly regarding phase.

The results presented in Figures 10 and 11 were based on the post-fit KBR residuals computed from the monthly mean solution of December 2004. The monthly mean solution of December 2004 includes 6 days of data after the earthquake, and thus, the obtained post-fit KBR residuals before the earthquake could be affected by coseismic and free oscillation signals. To examine this effect, we also computed the post-fit KBR residuals based on a sub-monthly mean solution from GRACE L1B data before the earthquake (i.e., from 1 to 25 December 2004) and repeated the same analyses as in Figures 10 and 11. We observed that the results were the same (not shown). Finally, our analysis to detect excitations in the frequency band of 1 and 5 CPR was polluted by other signals, resulting in difficulty to identify any possible evidence of the free oscillations.

6. Summary and Outlook

This paper, as the first attempt of its kind, investigated the problem of synthesizing and observing the gravitational signature of the Earth's free oscillations using GRACE satellites orbiting at ~500 km above the Earth's surface. Earth's free oscillations, excited by great earthquakes, generate transient gravitational potential changes that are predicted to be detected for as long as a few days. Thus, in contrast to coseismic and postseismic gravity changes that are conventionally studied using the GRACE L2 monthly mean gravity solutions, the transient gravitational signals are examined with a more fundamental observable of the instantaneous inter-satellite KBR (L1B data products) of the GRACE mission.

We employed the normal mode summation scheme to synthesize transient global gravity changes after the 2004 Sumatra earthquake. Quantification of surface gravity changes during the first 24 hr after the earthquake indicated excitations of as large as 2 mm and 4 μGal over a broad region in geoid and gravity disturbance, respectively. We showed that most of the high-frequency normal modes diminish significantly after a couple of hours and the largest excitations in surface gravity were found around the earthquake epicenter and its antipode. Evaluation of geoid changes due to individual gravest normal modes showed that the

football mode ${}_0S_2$ with a period of ~54 min and a Q of ~500 causes the largest excitations with a magnitude of 0.5 mm in geoid undulation over a few days.

Such transient gravitational potential changes cause perturbation in the trajectory of satellites orbiting around the Earth. Precise measurements of range change between two GRACE satellites are used to infer temporal variations in the Earth's global gravity field. However, analyzing inter-satellite range changes associated with free oscillations is not trivial due to the complicated coupling between the eigenfrequency of the modes, the Earth's rotation rate, and the angular velocity of satellites in the orbital plane. By extending the Kaula orbit perturbation theory, we developed an analytic model of how the gravitational potential of a spheroidal normal mode of degree l perturbs the GRACE orbit in terms of inter-satellite distance at $(2l+1) \times (l+1)$ distinct frequencies. For example, the ${}_0S_2$ mode excites gravitational perturbation at 15 different frequencies, regrouped in $l+1 = 3$ multiplets in the along-track KBR data. One group of five singlets are below 1 CPR, where there is a possibility of being distinguished from other geophysical perturbations. We validated our analytic model using results from the numerical orbit integration. It was found that the ${}_0S_2$ mode of the 2004 Sumatra earthquake is predicted to yield, through gravitational change, range-rate perturbation with a peak-to-peak variation of 0.5 μm/s at a period of roughly 12 hr. Our synthetic test for the 2004 Sumatra earthquake indicated that along-track excitations due to other gravest normal modes are within the actual error of GRACE KBR data.

We applied wavelet analysis to obtain 2-D time-frequency map of the actual GRACE KBR residual data in December 2004. A discernable transient signal was observed at the (predicted) frequency of ~0.022 mHz right after the 2004 Sumatra earthquake on 26 December from the time-frequency spectrum. According to our analytical model, it is known that the frequency of 0.022 mHz is the one associated with the largest excitation due to the football mode ${}_0S_2$. However, it seems that the large remaining error of the accelerometers at low frequencies (after calibration) interferes with the seismic gravitational signals particularly at frequencies lower than 1 CPR; this makes it difficult to distinguish the free oscillation signals from the GRACE accelerometer errors.

The recently-launched GRACE-FO mission has demonstrated inter-satellite ranging a few times better than GRACE using microwaves and ~20 times better using its laser ranging interferometer (Flechtner et al., 2014; Webb, 2018). The enhanced performance of inter-satellite ranging techniques may lead to reliable detection of not only lowest frequency (as shown in this study) but also higher frequency gravitational changes from a larger number of earthquakes of smaller magnitudes.

The gravitational perturbation by the ${}_0S_2$ mode of free oscillations is a non-negligible force even for higher altitude satellites such as LAGEOS and Starlette. We found that for the first 7 days following the 2004 Sumatra earthquake, the accelerations caused by free oscillations are noticeably above the expected non-conservative force model errors (Hedin, 1987; Knocke et al., 1988; Miliani et al., 1987; Rubincam, 1988); see Figure S8 and the relating text in the supporting information. This illustrates that the geodetic satellites, tracked by Satellite Laser Ranging (SLR), could contribute potentially to the estimation of the harmonic coefficients representing the free oscillations from great earthquakes provided the errors in the SLR data (e.g., Appleby et al., 2016), the Terrestrial Reference Frame (TRF), and force modeling could be properly accommodated.

Another proposed way of measuring gravitational changes of earthquakes from space is using the next-generation superconducting gravity gradiometer (SGG; Griggs et al., 2014; Griggs et al., 2017) with technology readiness level 4 and a gradiometer based on cold atom interferometry (Carraz et al., 2014). Specifically, the SGG uses stable persistent currents arising from absolutely stable quantized magnetic flux to cancel the common-mode acceleration of the spacecraft (such as atmospheric drag and solar radiation pressure). The tensor SGG measurement will not include the common-mode in all six degrees of freedom. The linear and angular acceleration exclusion is better at low frequencies because the acceleration itself becomes small at low frequencies. It will permit reliable measurements of the Earth's gravitational gradients at low frequency, leading to a favorable condition for detecting the Earth's free oscillations. A simulation analysis shows that gravitational gradient changes excited by ${}_0S_2$ could be 1 order of magnitude larger than the SGG instrument noise at lower frequencies (see Figure S9).

The satellite gravimetry techniques can provide “spatial” information of the free oscillation eigenmodes, while the ground-based gravimeters (point-wise measurements) can only provide information about the

frequency and damping of the excited modes. Both types of data are complementary and useful to constraining the Earth's interior structure, although it is uncertain how much "new" information the spaceborne detection of free oscillations may bring for the Earth's structure beyond the current knowledge from ground-borne seismic and gravimetric instruments.

Recently, transient gravitational perturbations were demonstrated to be useful in detecting earthquakes before the *P* wave arrival, and thus, helpful to earthquake early warning (Montagner et al., 2016; Vallée et al., 2017). These studies elaborated on modeling of earthquake-induced gravitational signals based on ground-borne seismometers (i.e., accelerometers) by considering the spontaneous gravitational force caused by ambient density perturbation and the inertial acceleration affecting the instrument housing. Both accelerations are generally of the same order of magnitude with the opposite sign (Juhel et al., 2018), yielding smaller acceleration measurements by seismometers. The satellite-borne measurements, on the other hand, are only sensitive to gravitational forces. On-going development of improved space-borne gravimetric sensors and proposed future satellite missions (Griggs et al., 2017; National Academies of Sciences, Engineering, and Medicine, 2018; Rakholia et al., 2017) will bring new kinds of global observations helpful to advancing our understanding of earthquakes and mitigating earthquake hazards.

Acknowledgments
This work is funded by The University of Newcastle to support NASA's GRACE and GRACE Follow-On projects as an international science team member to the missions, and by Australian Research Council (DP160104095 and DP170100224) as well as by NASA support to J. Sauber as a science team 660 member. We thank DLR for GRACE telemetry data and JPL, CSR, and GFZ for high-quality Level-1B and Level-2 data. We thank H. J. Paik and his team for providing us information on the intrinsic SGG noise, R. Riva for sharing the normal mode code for computing static change used for validation in Figure S1, and D. Rowlands and D. Chinn for SLR computation using the GEODYN software. The authors also would like to thank Paul Tregoning (Editor) and two anonymous reviewers for their constructive comments which led to a clearer presentation of our work. The GRACE data used in this study could be obtained from https://podaac.jpl.nasa.gov/GRACE or https://isdc.gfz-potsdam.de/grace-isdc/?L.

References

Aki, K., & Richards, P. G. (2002). *Quantitative seismology*. Sausalito, California: University Science Books.

Alterman, Z., Jarosch, H., & Pekeris, C. L. (1959). Oscillations of the Earth. *Proceedings of the Royal Society*, *252*(1268), 80–95. https://doi.org/10.1098/rspa.1959.0138

Appleby, G., Rodriguez, J., & Altamimi, Z. (2016). Assessment of the accuracy of global geodetic satellite laser ranging observations and estimated impact on ITRF scale: Estimation of systematic errors in LAGEOS observations 1993-2014. *Journal of Geodesy*, *90*(12), 1371–1388. https://doi.org/10.1007/s00190-016-0929-2

Benioff, H., Press, F., & Smith, S. (1961). Excitation of the free oscillations of the earth by earthquakes. *Journal of Geophysical Research*, *66*(2), 605–619. https://doi.org/10.1029/JZ066i002p00605

Bettadpur, S. (2009). Recommendation for a-priori bias scale parameters for Level-1B ACC data (Version 2). GRACE TN-02. Center for Space Research, The University of Texas at Austin.

Bettadpur, S. (2012). Gravity Recovery and Climate Experiment UTCSR Level-2 Processing Standards Document for Level-2 Product Release 0005, Center for Space Research. Uni. of Texas, Austin

Carraz, O., Siemes, C., Massotti, L., Haagmans, R., & Silvestrin, P. (2014). A spaceborne gravity gradiometer concept based on cold atom interferometers for measuring Earth's gravity field. *Microgravity Science and Technology*, *26*(3), 139–145. https://doi.org/10.1007/s12217-014-9385-x

Carrère, L., Lyard, F., Cancet, M., & Guillot, A. (2015). FES 2014, a new tidal model on the global ocean with enhanced accuracy in shallow seas and in the Arctic region. Paper presented at The EGU General Assembly, Venice.

Cazenave, A., & Chen, J. (2010). Time-variable gravity from space and present-day mass redistribution in theEarth system. *Earth and Planetary Science Letters*, *298*(3-4), 263–274. https://doi.org/10.1016/j.epsl.2010.07.035

Chao, B. F., Chung, W., Shih, Z., & Hsieh, Y. (2014). Earth's rotation variations: a wavelet analysis. *Terra Nova*, *26*(4), 260–264. https://doi.org/10.1111/ter.12094

Chao, B. F., & Gross, R. S. (1987). Changes in the Earth's rotation and low-degree gravitational field induced by earthquakes. *Geophysical Journal of the Royal Astronomical Society*, *91*(3), 569–596. https://doi.org/10.1111/j.1365-246X.1987.tb01659.x

Cheng, M. K. (2002). Gravitational perturbation theory for inter-satellite tracking. *Journal of Geodesy*, *76*(3), 169–185. https://doi.org/10.1007/s00190-001-0233-6

Dahlen, F. A. (1980). A uniformly valid asymptotic representation of normal mode multiplet spectra on a laterally heterogeneous Earth. *Geophysical Journal of the Royal Astronomical Society*, *62*(2), 225–247. https://doi.org/10.1111/j.1365-246X.1980.tb04853.x

De Linage, C., Rivera, L., Hinderer, J., Boy, J. P., Rogister, Y., Lambotte, S., & Biancale, R. (2009). Separation of coseismic and post-seismic gravity changes for the 2004 Sumatra–Andaman earthquake from 4.6 yr of GRACE observations and modelling of the coseismic change by normal-modes summation. *Geophysical Journal International*, *176*(3), 695–714. https://doi.org/10.1111/j.1365-246X.2008.04025.x

Ding, H., & Chao, B. F. (2015). The Slichter mode of the Earth: Revisit with optimal stacking and autoregressive methods on full superconducting gravimeter data set. *Journal of Geophysical Research: Solid Earth*, *120*, 7261–7272. https://doi.org/10.1002/2015JB012203

Dobslaw, H., Bergmann-Wolf, I., Forootan, E., Dahle, C., Mayer-Gürr, T., Kusche, J., & Flechtner, F. (2016). Modeling of present-day atmosphere and ocean non-tidal de-aliasing errors for future gravity mission simulations. *Journal of geodesy*, *90*(5), 423–436. https://doi.org/10.1007/s00190-015-0884-3

Dobslaw, H., Flechtner, F., Bergmann-Wolf, I., Dahle, C., Dill, R., Esselborn, S., et al. (2013). Simulating high-frequency atmosphere-ocean mass variability for dealiasing of satellite gravity observations: AOD1B RL05. *Journal of Geophysical Research: Oceans*, *118*, 3704–3711. https://doi.org/10.1002/jgrc.20271

Dziewonski, A. M., & Anderson, D. L. (1981). Preliminary reference Earth model. *Physics of the earth and planetary interiors*, *25*(4), 297–356. https://doi.org/10.1016/0031-9201(89)90055-1

Flechtner, F., Morton, P., Watkins, M., & Webb, F. (2014). Status of the GRACE follow-on mission. In U. Marti (Ed.), *Gravity, geoid and height systems*, (pp. 117–121). Springer, Cham. https://doi.org/10.1007/978-3-319-10837-7_15

Flury, J., Bettadpur, S., & Tapley, B. D. (2008). Precise accelerometry onboard the GRACE gravity field satellite mission. *Advances in Space Research*, *42*(8), 1414–1423. https://doi.org/10.1016/j.asr.2008.05.004

Gilbert, F. (1970). Excitation of the normal modes of the Earth by earthquake sources. *Geophysical Journal International*, *22*(2), 223–226. https://doi.org/10.1111/j.1365-246X.1971.tb03593.x

Gilbert, F., & Backus, G. E. (1966). Propagator matrices in elastic wave and vibration problems. *Geophysics*, *31*(2), 326–332. https://doi.org/10.1190/1.1439771

Gilbert, F., & Dziewonski, A. M. (1975). An application of normal mode theory to the retrieval of structural parameters and source mechanisms from seismic spectra. *Philosophical Transactions of the Royal Society A*, *278*(1280), 187–269. https://doi.org/10.1098/rsta.1975.0025

Griggs, C. E., Moody, M. V., Norton, R. S., Paik, H. J., & Venkateswara, K. (2017). Sensitive superconducting gravity gradiometer constructed with levitated test masses. *Physical Review Applied*, *8*(6), 064024. https://doi.org/10.1103/PhysRevApplied.8.064024

Griggs, C. E., Paik, H. J., Moody, M. V., Han, S.-C., Rowlands, D. D., Lemoine, F. G., & Shirron, P. J. (2014), Levitated superconducting gravity gradiometer for planetary missions, A paper presented at International Workshop on Instrumentation for Planetary Missions (IPM-2014), Greenbelt, Maryland, November 4-7, 2014, http://ssed.gsfc.nasa.gov/IPM/PDF/1021.pdf

Gross, R. S., & Chao, B. F. (2006). The rotational and gravitational signature of the December 26, 2004 Sumatran earthquake. *Surveys in Geophysics*, *27*(6), 615–632. https://doi.org/10.1007/s10712-006-9008-1

Han, S. C., Jekeli, C., & Shum, C. K. (2004). Time-variable aliasing effects of ocean tides, atmosphere, and continental water mass on monthly mean GRACE gravity field. *Journal of Geophysical Research*, *109*, B04403. https://doi.org/10.1029/2003JB002501

Han, S. C., Riva, R., Sauber, J., & Okal, E. (2013). Source parameter inversion for recent great earthquakes from a decade-long observation of global gravity fields. *Journal of Geophysical Research: Solid Earth*, *118*, 1240–1267. https://doi.org/10.1002/jgrb.50116

Han, S. C., Sauber, J., & Luthcke, S. (2010). Regional gravity decrease after the 2010 Maule (Chile) earthquake indicates large-scale mass redistribution. *Geophysical Research Letters*, *37*, L23307. https://doi.org/10.1029/2010GL045449

Han, S. C., Sauber, J., & Pollitz, F. (2015). Coseismic compression/dilatation and viscoelastic uplift/subsidence following the 2012 Indian Ocean earthquakes quantified from satellite gravity observations. *Geophysical Research Letters*, *42*, 3764–3772. https://doi.org/10.1002/2015GL063819

Han, S. C., Sauber, J., & Riva, R. (2011). Contribution of satellite gravimetry to understanding seismic source processes of the 2011 Tohoku-Oki earthquake. *Geophysical Research Letters*, *38*, L24312. https://doi.org/10.1029/2011GL049975

Han, S. C., Shum, C. K., Bevis, M., Ji, C., & Kuo, C. Y. (2006). Crustal dilatation observed by GRACE after the 2004 Sumatra-Andaman earthquake. *Science*, *313*(5787), 658–662. https://doi.org/10.1126/science.1128661

Hedin, A. E. (1987). MSIS-86 thermospheric model. *Journal of Geophysical Research*, *92*(A5), 4649–4662. https://doi.org/10.1029/JA092iA05p04649

Heiskanen, W. A., & Moritz, H. (1967). *Physical geodesy*. San Francisco: W H Freeman and Co.

Heki, K., & Matsuo, K. (2010). Coseismic gravity changes of the 2010 earthquake in central Chile from satellite gravimetry. *Geophysical Research Letters*, *37*, L24306. https://doi.org/10.1029/2010GL045335

Juhel, K., Montagner, J., Vallée, M., Ampuero, J., Barsuglia, M., Bernard, P., & Whiting, B. (2018). Normal mode simulation of prompt elastogravity signals induced by an earthquake rupture. *Geophysical Journal International*, *216*, 935–947. https://doi.org/10.1093/gji/ggy436

Kanamori, H., & Cipar, J. J. (1974). Focal process of the great Chilean earthquake May 22, 1960. *Physics of the Earth and Planetary Interiors*, *9*(2), 128–136. https://doi.org/10.1016/0031-9201(74)90029-6

Keller, W. (2004). *Wavelets in geodesy and geodynamics*. Walter de Gruyter. https://doi.org/10.1515/9783110198188

Kim, J. R. (2000). Simulation study of a low-low satellite-to-satellite tracking mission, (Dissertation). University of Texas at Austin, Austin.

Klinger, B., & Mayer-Gürr, T. (2016). The role of accelerometer data calibration within GRACE gravity field recovery: Results from ITSG-Grace2016. *Advances in Space Research*, *58*(9), 1597–1609. https://doi.org/10.1016/j.asr.2016.08.007

Knocke, P.J., Ries, J.C., & Tapley, B.D. (1988). Earth radiation pressure effects on satellites. In: Proceedings of the AIAA/AAS Astrodynamics Conference. Am. Inst. Aeron. Astronaut., Washington, D.C., pp. 577–587.

Kaula, W. M. (1966). *Theory of satellite geodesy*. Waltham: Blaisdel Publishing company.

Masters, G., Barmine, M. P., & Kientz, S. (2014). *Mineos user's manual*. Pasadena, Calif: Computational Infrastructure for Geodynamics. Calif. Inst. of Technol.

Masters, G., Jordan, T. H., Silver, P. G., & Gilbert, F. (1982). Aspherical Earth structure from fundamental spheroidal-mode data. *Nature*, *298*(5875), 609. https://doi.org/10.1038/298609a0

Mayer-Gürr, T., Behzadpour, S., Ellmer, M., Kvas, A., Klinger, B., Zehentner, N. (2016). ITSG-Grace2016 - Monthly and Daily Gravity Field Solutions from GRACE. GFZ Data Services. http://doi.org/10.5880/icgem.2016.007

Mayer-Gürr, T., Dobslaw, H., Kvas, A., & Poropat, L. (2018) Error budget of GRACE gravity field recovery – a simulation study. In: Proceedings of GRACE Science Team Meet, Potsdam

Mayer-Gürr, T., Pail, R., Gruber, T., Fecher, T., Rexer, M., Schuh, W.-D., et al. (2015). The combined satellite gravity field model GOCO05s. *Presented at EGU General Assembly 2015, Vienna, Austria, Geophysical Research Abstracts* (Vol. *17*). EGU2015-12364.

Mayer-Gürr, T., Savcenko, R., Bosch, W., Daras, I., Flechtner, F., & Dahle, C. (2012). Ocean tides from satellite altimetry and GRACE. *Journal of geodynamics*, *59-60*, 28–38. https://doi.org/10.1016/j.jog.2011.10.009

Montagner, J. P., Juhel, K., Barsuglia, M., Ampuero, J. P., Chassande-Mottin, E., Harms, J., et al. (2016). Prompt gravity signal induced by the 2011 Tohoku-Oki earthquake. *Nature Communications*, *7*(1), 13349. https://doi.org/10.1038/ncomms13349

National Academies of Sciences, Engineering, and Medicine (2018). *Thriving on our changing planet: A decadal strategy for Earth observation from space*. Washington, DC: The National Academies Press. https://doi.org/10.17226/24938

Ness, N. R., Harrison, C. T., & Slichter, L. B. (1961). Observation of the free oscillation of the earth. *Journal Geophysical Research*, *66*(2), 621–629. https://doi.org/10.1029/JZ066i002p00621

Nissen-Meyer, T., Dahlen, F. A., & Fournier, A. (2007). Spherical-earth Fréchet sensitivity kernels. *Geophysical Journal International*, *168*(3), 1051–1066. https://doi.org/10.1111/j.1365-246X.2006.03123.x

Okal, E. A., & Stein, S. (2009). Observations of ultra-long period normal modes from the 2004 Sumatra–Andaman earthquake. *Physics of the Earth and Planetary Interiors*, *175*(1-2), 53–62. https://doi.org/10.1016/j.pepi.2009.03.002

Olhede, S. C., & Walden, A. T. (2002). Generalized Morse wavelets. *IEEE Transactions on Signal Processing*, *50*(11), 2661–2670. https://doi.org/10.1109/TSP.2002.804066

Panet, I., Bonvalot, S., Narteau, C., Remy, D., & Lemoine, J. M. (2018). Migrating pattern of deformation prior to the Tohoku-Oki earthquake revealed by GRACE data. *Nature Geoscience*, *11*(5), 367. https://doi.org/10.1038/s41561-018-0099-3

Park, J., Song, T. R., Tromp, J., Okal, E., Stein, S., Roult, G., et al. (2005). Earth's free oscillations excited by the 26 December 2004 Sumatra-Andaman earthquake. *Science*, *308*(5725), 1139–1144. https://doi.org/10.1126/science.1112305

Piersanti, A., Spada, G., Sabadini, R., & Bonafede, M. (1995). Global postseismic deformation. *Geophysical Journal International*, *120*(3), 544–566. https://doi.org/10.1111/j.1365-246X.1995.tb01838.x

Pollitz, F. F. (1992). Postseismic relaxation theory on the spherical earth. *Bulletin of the Seismological Society of America*, *82*(1), 422–453.

Pollitz, F. F. (1996). Coseismic deformation from earthquake faulting on a layered spherical Earth. *Geophysical Journal International*, *125*(1), 1–14. https://doi.org/10.1111/j.1365-246X.1996.tb06530.x

Rakholia, A., Sugarbaker, A., Black, A., Kasevich, M., Saif, B., Luthcke, S., et al. (2017). Development of an atom interferometer gravity gradiometer for Earth sciences. A paper presented at the 48th Annual Meeting of the APS Division of Atomic, Molecular and Optical Physics, June 5–9, 2017; Sacramento, California, Abstract ID: BAPS.2017.DAMOP.K1.10. http://meetings.aps.org/link/BAPS.2017.DAMOP.K1.10

Ritzwoller, M. H., & Lavely, E. M. (1995). Three-dimensional seismic models of the Earth's mantle. *Reviews of Geophysics*, *33*(1), 1–66. https://doi.org/10.1029/94RG03020

Rosat, S., Sato, T., Imanishi, Y., Hinderer, J., Tamura, Y., McQueen, H., & Ohashi, M. (2005). High-resolution analysis of the gravest seismic normal modes after the 2004 Mw= 9 Sumatra earthquake using superconducting gravimeter data. *Geophysical Research Letters*, *32*, L13304. https://doi.org/10.1029/2005GL023128

Rubincam, D. P. (1988). Yarokovsky thermal drag on LAGEOS. *Journal of Geophysical Research*, *93*(B11), 13805–13810. https://doi.org/10.1029/JB093iB11p13805

Rosborough, G. W. (1986). Satellite orbit perturbations due to the geopotential. Tech. Rep. CSR-86-1, Center for Space research. University of Texas at Austin

Saito, M. (1967). Excitation of free oscillations and surface waves by a point source in a vertically heterogeneous earth. *Journal of Geophysical Research*, *72*(14), 3689–3699. https://doi.org/10.1029/JZ072i014p03689

Savcenko, R., and W. Bosch (2012), EOT11a—Empirical ocean tide model from multi-mission satellite altimetry, DGFI Report No. 89, Deutsches Geodätisches Forschungsinstitut, München.

Schrama, E. J. O. (1989). *The role of orbit errors in processing of satellite altimeter data*, *New Series 33, Netherlands Geodetic Commission*, (). Publications on Geodesy.

Smylie, D. E., & Mansinha, L. (1971). The elastic theory of dislocations in real Earth models and changes in the rotation of the Earth. *Geophysical Journal International*, *23*(3), 329–354. https://doi.org/10.1111/j.1365-246X.1971.tb01824.x

Sneeuw, N. (1992). Representation coefficients and their use in satellite geodesy. *Manuscripta geodaetica*, *17*, 117–123.

Sneeuw, N. (2000). A semi-analytical approach to gravity field analysis from satellite observations. C-527, Deutsche Geodätische Kommission, München. https://mediatum.ub.tum.de/601028

Stein, S., & Geller, R. J. (1977). Amplitudes of the Earth's split normal modes. *Journal of Physics of the Earth*, *25*(2), 117–142. https://doi.org/10.4294/jpe1952.25.117

Stein, S., & Okal, E. A. (2005). Speed and size of the Sumatra earthquake. *Nature*, *434*(7033), 581. https://doi.org/10.1038/434581a

Tapley, B. D., Bettadpur, S., Ries, J. C., Thompson, P. F., & Watkins, M. M. (2004). GRACE measurements of mass variability in the Earth system. *Science*, *305*(5683), 503–505. https://doi.org/10.1126/science.1099192

Vallée, M., Ampuero, J. P., Juhel, K., Bernard, P., Montagner, J. P., & Barsuglia, M. (2017). Observations and modeling of the elastogravity signals preceding direct seismic waves. *Science*, *358*(6367), 1164–1168. https://doi, https://doi.org/10.1126/science.aao0746

Visser, P. N. A. M. (2005). Low-low satellite-to-satellite tracking: a comparison between analytical linear orbit perturbation theory and numerical integration. *Journal of Geodesy*, *79*(1-3), 160–166. https://doi.org/10.1007/s00190-005-0455-0

Wagner, C., McAdoo, D., Klokočník, J., & Kostelecký, J. (2006). Degradation of geopotential recovery from short repeat-cycle orbits: Application to GRACE monthly fields. *Journal of Geodesy*, *80*(2), 94–103. https://doi.org/10.1007/s00190-006-0036-x

Wagner, C. A. (1987). Improved gravitational recovery from a geopotential research mission satellite pair flying en echelon. *Journal of Geophysical Research*, *92*(B8), 8147–8155. https://doi.org/10.1029/JB092iB08p08147

Webb, F. (2018), GRACE-FO mission status and further plans. A paper presented at GRACE/GRACE-FO Science Team Meeting, Helmholtz Centre Potsdam - GFZ German Research Centre for Geosciences, 9-11 October 2018

Wells, D. E., Vaníček, P., & Pagiatakis, S. D. (1985) Least squares spectral analysis revisited. Technical Report 84, Department of Surveying Engineering, University of New Brunswick, Canada

Wigner, E. (1959). *Group theory and its application to the quantum mechanics of atomic spectra*. New York: Academic Press.

Woodhouse, J. H. (1980). The coupling and attenuation of nearly resonant multiplets in the Earth's free oscillation spectrum. *Geophysical Journal International*, *61*(2), 261–283. https://doi.org/10.1111/j.1365-246X.1980.tb04317.x

Woodhouse, J. H., & Deuss, A. (2007). Theory and observations—Earth's free oscillations. In *Treatise on Geophysics, Vol. 1: Seismology and Structure of the Earth*, (pp. 31–65). New York: Elsevier.